SPACE WEATHER, VOL. 7, S05002, doi:10.1029/2008SW000409, 2009

Studying geoeffective interplanetary coronal mass ejections between the Sun and Earth: Space weather implications of Solar Mass Ejection Imager observations

D. F. Webb,[1,2] T. A. Howard,[3] C. D. Fry,[4] T. A. Kuchar,[1,2] D. R. Mizuno,[1,2]
J. C. Johnston,[2] and B. V. Jackson[5]

Received 30 April 2008; revised 26 September 2008; accepted 18 October 2008; published 14 May 2009.

[1] Interplanetary coronal mass ejections (ICMEs) are the primary cause of severe space weather at Earth because they drive shocks and trigger geomagnetic storms that can damage spacecraft and ground-based systems. The Solar Mass Ejection Imager (SMEI) is a U. S. Air Force experiment with the ability to track ICMEs in white light from near the Sun to Earth and beyond, thus providing an extended observational range for forecasting storms. We summarize several studies of SMEI's detection and tracking capability, especially of the ICMEs associated with the intense (peak $Dst \leq -100$ nT) geomagnetic storms that were the focus of the NASA Living With a Star Geostorm Coordinated Data Analysis Workshop. We describe the SMEI observations and analyses for the 18 intense storms observed from May 2003–2007 with adequate SMEI coverage and identified solar and interplanetary source regions. SMEI observed the associated ICMEs for 89% of these intense storms. For each event we extracted the time differences between these sets of times at 1 AU for shock arrival time, predicted ICME arrival time, onset of high-altitude aurora observed by SMEI, and storm onset. The mean intervals between successive pairs of these data were found to each be ~4 hours. On average, SMEI first detected the geoeffective ICME about 1 day in advance, yielding a prediction lead time of ~18 hours. Finally, the RMS values for the ICME-shock and storm-ICME time differences were determined, and provide at least a 1-hour improvement compared to similar observational and model-dependent studies.

Citation: Webb, D. F., T. A. Howard, C. D. Fry, T. A. Kuchar, D. R. Mizuno, J. C. Johnston, and B. V. Jackson (2009), Studying geoeffective interplanetary coronal mass ejections between the Sun and Earth: Space weather implications of Solar Mass Ejection Imager observations, *Space Weather*, *7*, S05002, doi:10.1029/2008SW000409.

1. Introduction

[2] Coronal mass ejections (CMEs), which are termed interplanetary coronal mass ejections (ICMEs) when they traverse interplanetary (IP) space, are the primary source of severe space weather at Earth. They cause geomagnetic storms that can damage both military and civilian, space and ground assets. These hazardous storms are difficult to forecast and there are many false alarms [e.g., *McKenna-Lawlor et al.*, 2006]. The Solar Mass Ejection Imager (SMEI) experiment [*Eyles et al.*, 2003; *Jackson et al.*, 2004] on the Coriolis spacecraft has been obtaining white light images of nearly the full sky every 102 min for the last 5 years. SMEI views the sky above Earth using sunlight-rejecting baffles and charge-coupled device (CCD) camera technology. When fully calibrated, sky maps of structures having enhanced electron density in the inner heliosphere can be produced. Over its 5-year lifetime, SMEI has observed over 300 ICMEs traveling through the inner heliosphere. *Webb et al.* [2006a] summarized the SMEI observations of ICMEs during the first 1.5 years of the mission. At least 25 of these transients, typically observed as frontside halo events by the SOHO Large Angle Spectroscopic Coronagraph (LASCO), were observed by SMEI propagating to and beyond 1 AU, and were associated with major geomagnetic storms at Earth.

---

[1] Institute for Scientific Research, Boston College, Chestnut Hill, Massachusetts, USA.

[2] Space Vehicles Directorate, Air Force Research Laboratory, Hanscom Air Force Base, Massachusetts, USA.

[3] Air Force Research Laboratory, National Solar Observatory, Sunspot, New Mexico, USA.

[4] Exploration Physics International, Inc., Huntsville, Alabama, USA.

[5] Center for Astrophysics and Space Science, University of California, San Diego, La Jolla, California, USA.

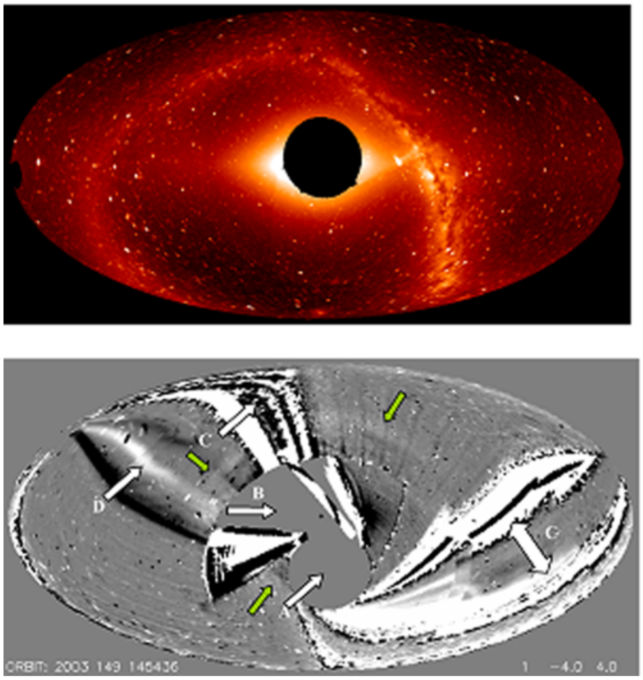

Figure 1. (top) SMEI all-sky Aitoff sky map. (bottom) A single-orbit difference image showing both a ICME (shaded arrows) and the main obscuration effects viewed by SMEI (open arrows). Lettered arrows are missing data resulting from A, the zone of exclusion near Sun; B, three camera frames that are shuttered because of bright sunlight (adjacent white-black areas have sunlight-saturated CCD pixels that are not bright enough to close the shutter); C, particle enhancements from both the polar zones and SAA; and D, auroral light. The ICME appears as arcs seen in three unobscured areas of the inner heliosphere. This was the first earthward-directed halo ICME observed by SMEI on 29 May 2003 (see Figure 2 and 3).

[3] The successful operation of SMEI is an important step toward demonstrating improved space weather forecasts. Early detection of potentially damaging Earth-directed ICMEs can help protect space assets and maintain stable communications. A geomagnetic storm initiates a wide variety of adverse effects, including increases in trapped magnetospheric particles, degraded satellite communication and surveillance systems, increased drag and deterioration of satellite altitude control, and destructive surges in ground power grids. For example, the ''Halloween'' storms in October–November 2003 caused everything from power grid failures to satellite shut downs (see *Webb and Allen* [2004] for a list of anomalies).

[4] SMEI's mission as an Air Force experiment is to demonstrate the ability to detect and track ICMEs from near the Sun to Earth, thus providing a new capability for forecasting the occurrence of storms. SMEI has accomplished this by detecting a number of geoeffective ICMEs at elongations of 20–30° (from Sun center), or estimated distances as far away as 2/3 of the distance between the Sun and Earth. Depending on the speed of the ICME front, these distances would correspond to lead times of 10 hours to 1–2 days. SMEI was not designed to be an operational mission, so most SMEI forecasts were retrospective, with a couple of exceptions (examples of real-time SMEI forecasts are noted in section 4.2.2). But these results do prove the principle that SMEI could detect even fast Earthward ICMEs <1 day before their Earth arrival and, thus, that a similar system, with automated event detection and/or 24/7 operator mon-

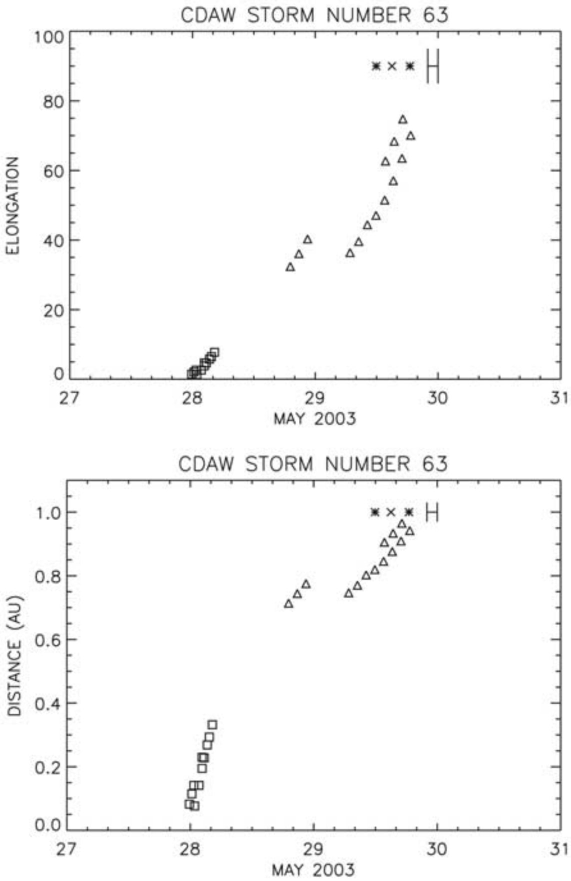

Figure 2. The 29–30 May 2003 ICME (Figure 1 (bottom)). CDAW storm 63 (top) elongation versus time and (bottom) distance versus time plots. See Figure 3. The symbols are as follows: squares, leading edge of CMEs in LASCO C2 and C3; triangles, leading edge of ICMEs in SMEI; asterisks, shock ATs at L1 at ACE or Wind (Shock Date and Time column of Table 2); crosses, SMEI aurora onset time (Aurora Date column of Table 2); vertical bars, storm onset and peak times (*Dst* Date column of Table 2). The $d-t$ data is used to calculate the arrival times of the ICME at 1 AU based on linear fits to the three separately tracked SMEI features; the two later ATs are given in Predicted 3-D column of Table 2.

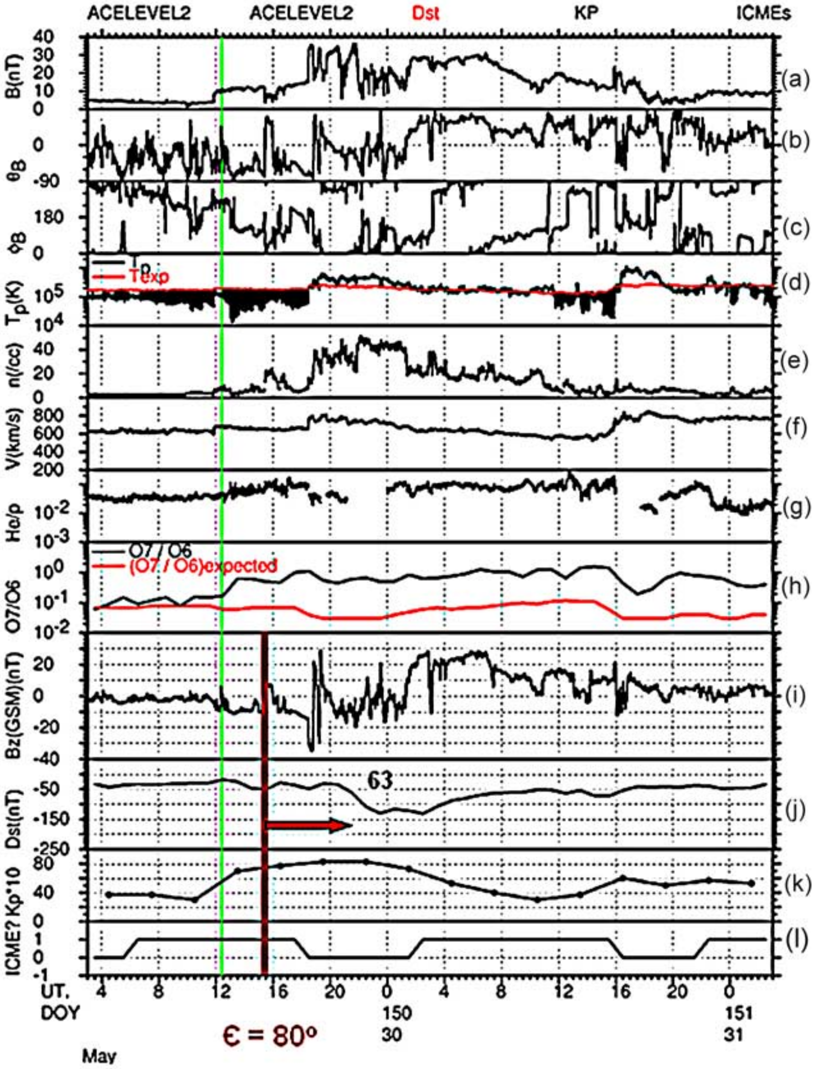

Figure 3. ACE solar wind and geomagnetic data during this period, from 29 to 31 May, for the 29–30 May 2003 ICME (Figure 1b; CDAW storm 63). The plot shows (a) the magnetic field intensity, the (b) polar and (c) azimuthal IMF components, (d) the solar wind proton temperature (black) and expected proton temperature (red) with the black shading indicating where the proton temperature falls below the expected temperature, (e) the proton density, (f) velocity, (g) helium/proton ratio, (h) the observed and expected O7/O6 ratio, (i) the B_z component of the IMF in GSM coordinates, the (j) *Dst* and (k) *Kp* geoindices, and (l) a 0/1 value indicating whether or not the signatures suggest an ICME flow [e.g., *Richardson and Cane*, 2004]. The vertical red bar indicates the onset time of bright aurora in SMEI (arrow) when the ICME front was at an elongation of 80°. The vertical green line indicates the AT of the first shock at ACE. ACE plot courtesy of I. Richardson.

itoring, and adequate data latency would constitute a reliable tool for early warning of storms.

[5] The first Earth-directed ICME detected and analyzed in the SMEI data occurred in late May 2003 [*Tappin et al.*, 2004] (Figures 1–3). This fast (projected speed of 1000 km/s) event was detected at ~30° elongation, about 15 hours before it passed over the Earth on 29–30 May causing a major geomagnetic storm. SMEI also observed ICMEs associated with a series of large solar events during 2 weeks in late October and early November 2003. These led to high levels of energetic particles in geospace and produced overlapping large geomagnetic storms on 29–30 October. The 28 and 29 October flares had peak X-ray fluxes among the largest ever recorded, shock waves among the fastest

ever observed, and two intense storms among the 14 strongest storms dating back to 1936. SMEI observed the first of these halo ICME events, again starting at distances about 1/3 of the way from the Sun to Earth, 10 hours before Earth arrival.

[6] The focus of this paper is on comparison of the SMEI ICME observations with the intense geomagnetic storms that were the focus of the NASA Living With a Star (LWS) Geostorm Coordinated Data Analysis Workshop (CDAW). This CDAW brought together scientists from many LWS disciplines to interact and collaborate on questions related to CMEs, ICMEs, and their connections to geomagnetic and ionospheric storms. The focal point of the CDAW was the set of all major geomagnetic storms (defined as having a peak $Dst \leq -100$ nT) of cycle 23, during the SOHO era from 1996 to 2004. Two Geostorm CDAWs were held, in 2005 and 2007; the purpose of the second was to extend the list of storms through 2005 and to have a scientific meeting to present first results. The data and some preliminary results from the CDAWs are available online at http://cdaw.gsfc.nasa.gov/geomag_cdaw/, especially under "Data" and "Resources."

[7] There were four CDAW working groups; working group 1 (WG1) on Drivers of Geomagnetic Storms, WG2 on Geomagnetic Storm Mechanisms, WG3 on Ionospheric Storms, and WG4 on Prediction of Geomagnetic Storms. The main goal of WG1 was to try to identify and categorize the solar and interplanetary sources of each of the intense storms. The major results of this process were presented by *Zhang et al.* [2007a, 2007b]. A second paper by *Richardson et al.* [2006, 2007] summarized results for the ten storms that were associated with corotating interaction regions (CIRs). Since initiating operations in February 2003, SMEI was able to observe the associated ICMEs for 89% of the intense storms. Here we describe the SMEI observations and analyses for the 26 CDAW storms that occurred during the SMEI observations from May 2003 to September 2005, as well as the two other intense storms that occurred after that period through the end of 2007.

[8] In section 2 we summarize the SMEI mission, emphasizing its observations of ICMEs that were likely directed toward the vicinity of the Earth. In section 3 we describe the main results comparing the SMEI ICME observations with the intense storms, and in section 4 the implications of the SMEI results for the forecasting of such storms at Earth. The results are summarized and discussed in section 5.

2. SMEI Mission and How We Identify Earthward ICMEs

2.1. SMEI Background

[9] SMEI was launched in January 2003 on the Air Force Space Test Program's Coriolis satellite. Coriolis is in a dawn-dusk, Sun-synchronous, circular polar orbit along the Earth's terminator at an altitude of 840 km and an inclination of 98° relative to the equatorial plane, and maintains a zenith-nadir orientation. SMEI has three baffled cameras, each covering a narrow 3° × 60° strip of the sky. Camera 1 points to the night sky, Camera 2 is centered on the terminator and Camera 3 points near the Sun. The cameras are mounted on the satellite with their fields of view (FOV) aligned end to end and slightly overlapping, so that the FOV swath is a 3° wide strip extending 160° along an approximate great circle with the ends near the orbit axis. Each camera takes continuous 4-s exposures in broadband white light during each orbit with 14 orbits per day. Since the cameras are fixed to the spacecraft, they image nearly 90% of the entire sky during each orbit. Gaps in coverage include a zone of exclusion of ~20° radius about the sunward orbital pole, a smaller circle in the opposite direction, and occasional areas shuttered because of sunlight in the sunward camera. The instrument operates continuously, so the primary data product comprises a sequence of 14 all-sky images per day. It has maintained a duty cycle of 85%, interrupted only for periodic calibration and diagnostic purposes and occasional software anomalies and telemetry problems. SMEI views the outward flow of density structures emanating from the Sun by observing Thomson-scattered sunlight from heliospheric plasma. The primary objective of SMEI is to demonstrate the feasibility of using such instrumentation to forecast the arrival of the ICMEs at Earth. SMEI has achieved this goal by imaging nearly the entire sky every 102 min, the spacecraft's orbital period, with sufficient sensitivity and photometric stability to be able to detect faint transient disturbances against the much brighter, but relatively unchanging stellar and zodiacal backgrounds.

[10] The individual 3° × 60° data frames are combined on the ground to form composite heliospheric all-sky maps. We typically use two types of Sun-centered projection: an equal-area Hammer-Aitoff projection and an angular "fisheye" projection wherein the distance from the center of the image is proportional to the angle from the camera view direction. An Aitoff sky map provides a reasonably undistorted representation of the sunward hemisphere, where most heliospheric disturbances are best observed, but at the cost of more serious distortion around the perimeter of the image region. Figure 1 (top) shows an Aitoff sky map, with ecliptic north at the top and east to the left. Fisheye projections (Figure 5 shows an example) have relatively little distortion out to ~100° elongation from the Sun and are particularly effective in following Earth-directed events.

[11] Details of the SMEI data handling, processing, background light subtraction and sky map production, particularly their pertinence for observing ICMEs, are discussed by *Jackson et al.* [2004] and *Webb et al.* [2006a]. Basically, SMEI is designed to measure heliospheric Thomson-scattered light integrated along each line of sight, like any white light coronagraph. Since the brightness of this emission falls off rapidly with distance from the Sun, care is needed in generating the full-sky SMEI images to insure that the variations in brightness from these very faint signals are detectable over the entire sky.

[12] There are a number of artifacts or backgrounds that can affect the SMEI sky maps. When a SMEI camera points close to the Sun, sunlight illuminates inner portions of the baffle and can saturate the CCD exposure. The sunward edge of the Camera 3 FOV is offset 20° from the sunward pole of the orbital plane creating a circular zone of avoidance ~20° in radius on the orbit maps. Because Coriolis is in a Sun-synchronous orbit and not Sun pointed, this exclusion zone moves north and south of Sun center during the year. To protect the CCD, a shutter in the light path closes when the solar illumination is too high. The sunward Camera 3 operates at much higher temperatures than intended, lowering its overall sensitivity primarily because of particle-induced radiation damage on the CCD. The background from individual stars, the extended emission from the Galactic plane, and the zodiacal light are each far brighter than the faint heliospheric structures (ICMEs) that SMEI is designed to detect. Other artifacts include the residuals from bright stars, data dropouts, and saturated regions due to the Moon and bright planets. Another artifact that is caused by the interactions of trapped radiation belt particles with the CCD and its processing electronics occurs on nearly every orbit and can affect large numbers of CCD pixels. These particles typically appear as the satellite crosses the polar auroral zones and during passages through the South Atlantic Anomaly (SAA). On the maps these regions appear as large area bands that have a granular appearance.

[13] Another type of "background" is an occasional visible light phenomenon associated with the geoaurora [*Mizuno et al.*, 2005]. This phenomenon occurs in the auroral zones and polar regions above Coriolis's orbit (>840 km); SMEI's observations of this high-altitude aurora were unanticipated and constitute a major discovery. This auroral light viewed by SMEI can be very bright, and it is well correlated in both brightness and frequency with periods of enhanced geomagnetic activity when the indices *Kp* and *Dst* have peak values $>\sim 6$ and ≤ -60 nT, respectively. As such it has proven to be of great value from a space weather perspective in identifying the time of arrival of geoeffective shocks and ejecta and the onset and duration of the associated storms.

[14] Figure 1 (bottom) illustrates these artifacts (except for the moon) along with a true ICME on an orbital difference image. The open lettered arrows point to the artifacts. The ICME (shaded arrows) appears as arcs in three unobscured areas of the inner heliosphere. This was the first Earthward-directed halo ICME observed by SMEI, on 29 May 2003.

2.2. Identifying Earthward ICMEs in SMEI

[15] The primary backgrounds, which are from individual stars, the Galactic plane emission and the zodiacal light, can be removed to first order by producing orbital difference images, so-called "running differences." In effect, a constant heliospheric signal cancels out in the difference map, leaving only the changes in heliospheric structures from one orbit to the next. We found that ICMEs are usually too faint to be detectable on the direct maps or movies made from them, but become readily observable as moving structures on the difference movies. More advanced techniques are being developed at UCSD and AFRL to remove these background signals and better calibrate the SMEI data [e.g., *Jackson et al.*, 2006; *Hick et al.*, 2005]. Such processed sky maps have now been produced for most of the SMEI mission and are being used in the data analysis on a case-by-case basis. We have used these images and movies to analyze the storm events herein.

[16] *Webb et al.* [2006a] analyzed the SMEI observations of ICMEs for the first 1.5 years of the SMEI mission. The SMEI ICME occurrence rate was about 1/3 CMEs/day, about an order of magnitude less than the LASCO CME rate for the same time period. Thus, SMEI sees only a fraction of all eruptions identified as CMEs in the LASCO data, and we are currently comparing CMEs/ICMEs observed with both instruments to characterize the differences. Some reasons for the lower SMEI rate are that SMEI is less sensitive to CMEs erupting off the backside of the Sun because of Thomson scattering at these large elongations, and frequent, multiple CMEs can merge at large distances from the Sun. Recently, *Howard and Simnett* [2008] examined appropriate LASCO data for evidence of CMEs corresponding to 189 SMEI events observed from February 2003 to September 2005. Of those SMEI ICMEs, 143 (76%) were associated with one or more LASCO CMEs, 31 (16%) were only weakly associated with LASCO activity, and 15 (8%) had no apparent LASCO activity. That SMEI observes ICME material in the inner heliosphere that is not visible near the Sun is an important finding that is currently under study.

[17] *Webb et al.* [2006a] reported that the average duration of SMEI ICMEs was ~16 hours with a maximum of about three days. The SMEI ICME angular spans or widths averaged 42°, ranging up to 107°, but this is a lower limit because of obscuration of the sides of many ICMEs. The average peak brightness of a SMEI ICME was 2.3 S10 units (an S10 unit is the equivalent flux of 10th magnitude, solar-type stars per square degree). The maximum observed elongation to which SMEI could track ICMEs was ~145°. The SMEI ICMEs could be grouped into seven interpretative categories, of which the most common were limb ICMEs, distant wide arcs and Earthward-directed ICMEs. The latter are of the most interest for this paper.

[18] Figures 4a–4d are an example of the limb ICME class, one of two similar, fast, west limb loop events likely associated with NOAA active region 0365, the region associated with the earlier 28–29 May 2003 halo ICME (Figures 1–3) when the active region was near Sun center. The limb event on 31 May led to a circular loop CME seen in LASCO C2 and C3 images (inset) and the SMEI ICME. The loop's location and width (~60°) were similar in both the LASCO and SMEI views. Figure 4e is the elongation versus time plot of the ICME front. Assuming projection in the skyplane, the speeds of the front calculated from the

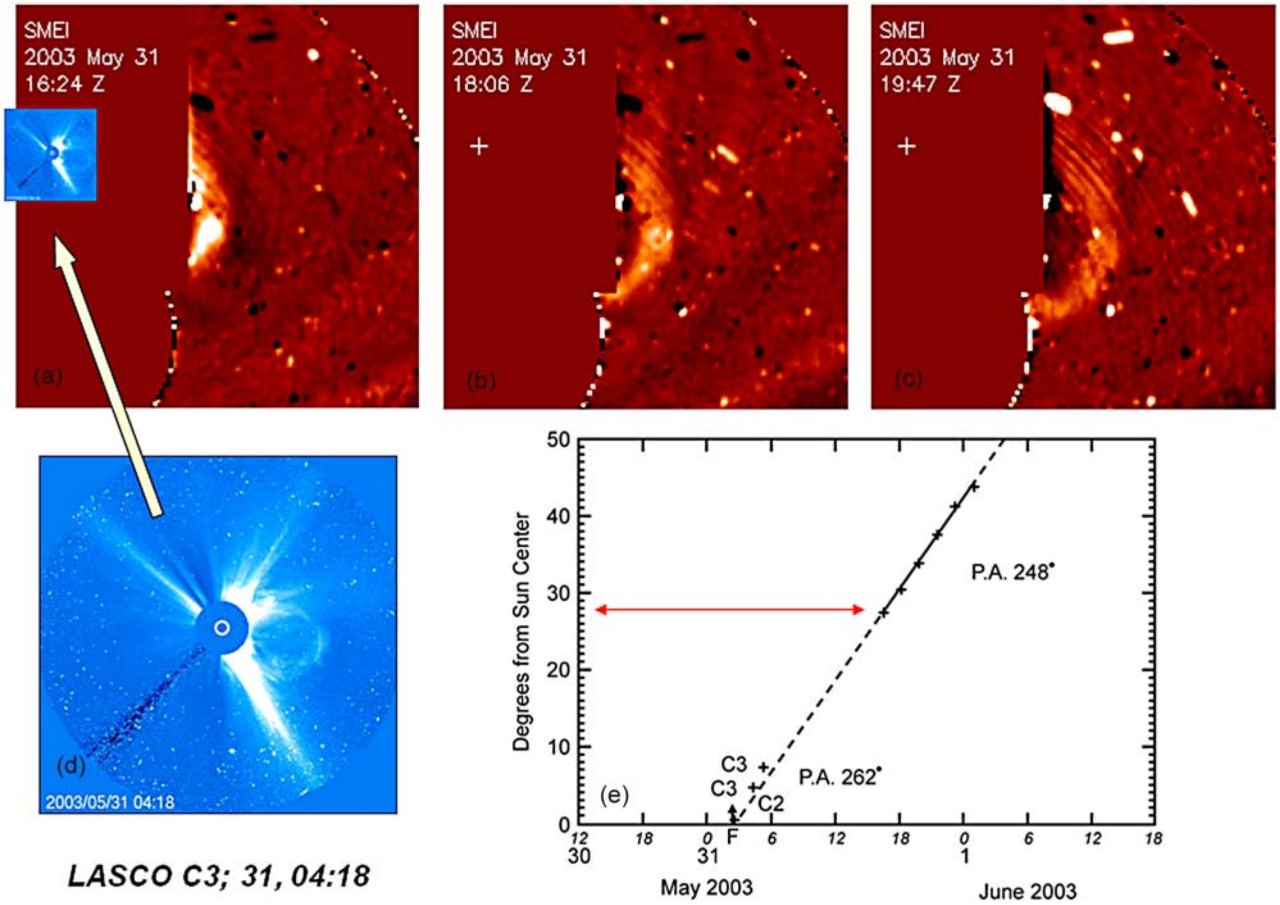

Figure 4. (a–d) Example of a loop CME viewed off the solar limb by LASCO (blue) and SMEI Camera 3 (red). The event on 31 May 2003 was associated with a 2B, M9.3 flare with onset at 0215 UT and disk location S07°W65°. This led to a circular loop CME seen in LASCO (C3 image in inset). (e) Elongation versus time plot of the ICME front seen in SMEI with $27° < \varepsilon < 44°$. The linear fit extrapolation earlier in time matches well with the flare (F) onset and LASCO C2, C3 height times. From *Webb et al.* [2006a].

LASCO (1830 km/s) and SMEI (~1450 km/s) data agree reasonably well. These events illustrate that at least some ICMEs appear to undergo little change as they propagate outward from their low coronal origins, in this case out to 45° elongation. Such bright, relatively fast ICMEs occurring near the solar limb are fairly easy to detect in SMEI's sunward camera and to correlate with solar surface events and LASCO CMEs. This is because the intensity of light emitted via the Thomson scattering process is maximized for plasma that is closest to the Sun along the line of sight. However, in the SMEI images such limb CMEs fade rapidly as they move outward, as expected for Thomson scattering [see, e.g., *Vourlidas and Howard*, 2006]. Likewise, this effect implies that SMEI will not detect much, if any emission from events ejected from the backside of the Sun.

[19] The distant arc events are fairly common, though often faint and subtle in individual frames, and comprise about 1/3 of all the SMEI events. Because of the Thomson-scattering geometry, these distant arcs could either be directed toward the Earthward hemisphere of the sky or in some cases could be near Earth. Typical examples are the events in Figures 5 and 6. The arc shown in Figure 5a swept beyond 90° elongation through Camera 2, which is centered on the terminator, into Camera 1, thus from the dayside into the night sky, at about the time a geomagnetic storm began. Such terminator-crossing events are best observed in the southeast quadrant of the SMEI FOV, where the obscuration from particles in the auroral zones and the SAA are minimal.

[20] Since ICMEs are the primary cause of major space weather events, such as storms and particle enhancements, it is important to be able to detect and track their fronts as they propagate through the inner heliosphere toward Earth. Until the launch of SMEI, forecasters had almost no information on the movement of a geoeffective ICME once it left the FOV of a coronagraph, such as the LASCO

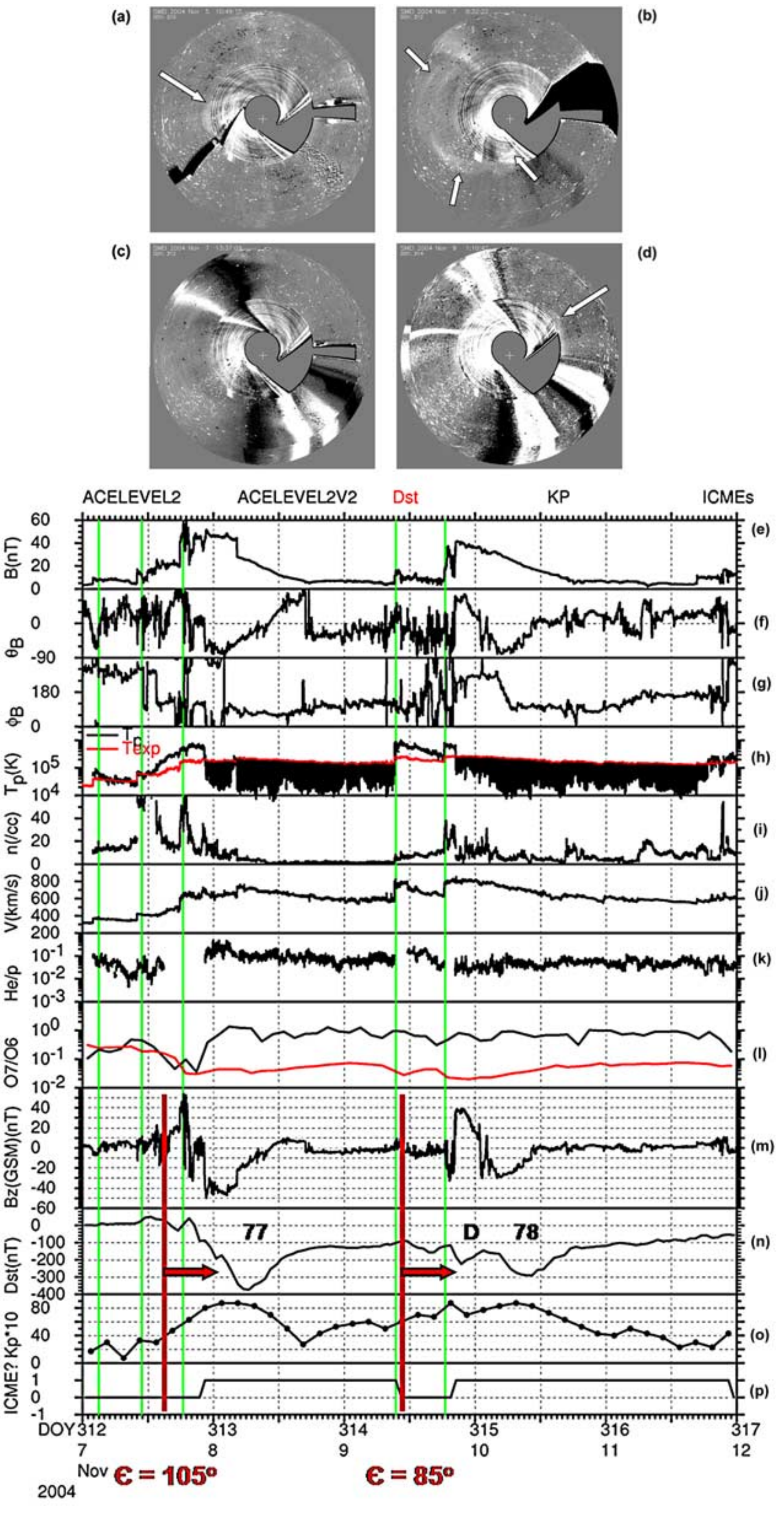
(a)
(b)
(c)
(d)
ACELEVEL2
ACELEVEL2V2
Dst
KP
ICMEs
B(nT)
60
40
20
0
(e)
θB
0
-90
(f)
φB
180
0
(g)
Tp
TExp
Tp(K)
10^5
10^4
(h)
n(/cc)
40
20
0
(i)
V(km/s)
800
600
400
200
(j)
He/p
10^-1
10^-2
10^-3
(k)
O7/O6
10^0
10^-1
10^-2
(l)
Bz(GSM)(nT)
40
20
0
-20
-40
-60
(m)
Dst(nT)
0
-100
-200
-300
-400
77
D
78
(n)
Kp*10
80
40
0
(o)
ICME?
1
0
-1
(p)
DOY 312
313
314
315
316
317
7
8
9
10
11
12
Nov
2004
ϵ = 105°
ϵ = 85°

Figure 5

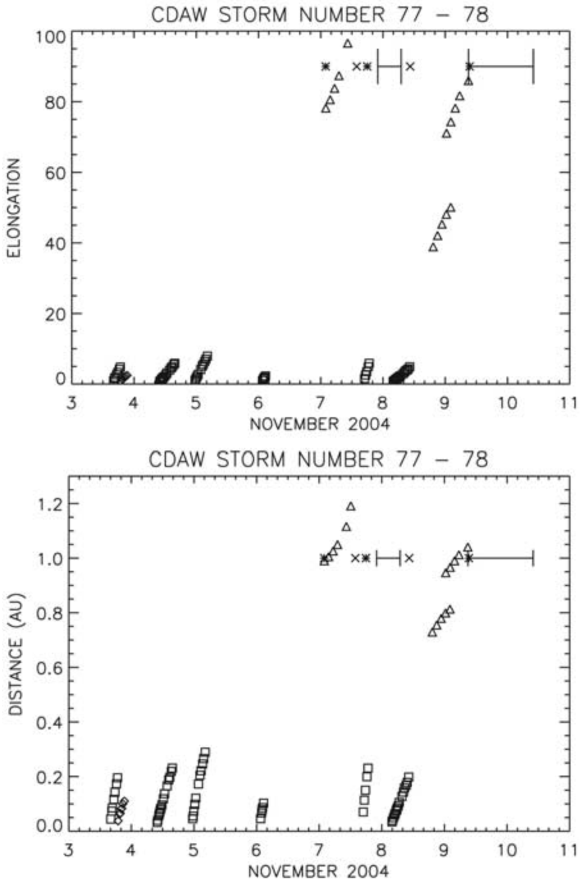

Figure 6. The 3–10 November 2004 LASCO CMEs, SMEI ICMEs (Figure 5), and time markers at 1 AU for CDAW storms 77 and 78. (top) Elongation-time plot and (bottom) distance-time plot. Symbols are the same as in Figure 2.

C3 which views to a radius of 7.5°, or 30 R_S, from the Sun. Forecasters, however, have been aided by LASCO's ability to frequently observe halo CMEs. Such CMEs appear as a bright ring surrounding the occulter indicating their direction along the Sun-Earth line; additional observations of frontside surface activity are used to indicate whether it is Earth directed. Several radio techniques have been used to remotely detect and track disturbances in the interplanetary medium. These are kilometric radio observations from space and interplanetary scintillation (IPS) observations from the ground. The kilometric observations can track the emission typically only from strong shocks traveling ahead of fast ICMEs. The IPS technique suffers from relatively poor temporal (~24 hours) and spatial resolution, ionospheric noise, and a model dependence for interpreting the signal as density or mass.

[21] SMEI has now observed at least 30 ICMEs that were likely directed toward the general vicinity of Earth. These are typically a subset of the arc-like category of events. Those most likely Earth directed have these characteristics: (1) They are associated with solar activity near Sun center and with LASCO halo CMEs; (2) they tend to be arc-like and wide, with spans on the order of 60°; (3) the arcs appear to sweep by Earth's terminator from the dayside into the night side, i.e., they move across the Camera 2 FOV; and (4) the timing of this terminator passage tends to correspond to the onset of auroral brightening in SMEI. Examples of such events are shown in Figures 1, 5, and 11.

3. Review of Prior Studies Comparing SMEI ICMEs With Geomagnetic Storms

[22] There have been several previous studies comparing SMEI ICMEs with geomagnetic storms that are pertinent to this paper. Since not all of these studies have been published, we summarize their results in this section. The studies are grouped into three topical areas. The common study among all three is *Howard et al.*'s [2006] study of 20 SMEI ICMEs compared with shocks at ACE at L1. That study was basically the precursor to this paper.

3.1. Association of SMEI ICMEs With Moderate to Major Storms

[23] Two preliminary and independent studies were made of SMEI's capability to detect and track ICMEs that subsequently caused major storms at Earth. These results

Figure 5. SMEI ICMEs (CDAW storms 77 and 78). Four views of SMEI ICMEs in orbit difference images ((a) 5 November 2004 at 1049 UT, first loop appears to east (arrow) in Cameras 3 and 2; (b) 7 November 2004 at 0832 UT, two arcs near Earth (arrows); (c) 7 November 2004 at 1337 UT, onset of aurora (large black and white areas in upper left and lower right); and (d) 9 November 2004 at 0110 UT, loop to northwest (arrow) in Camera 2). The plus sign marks the Sun's location. Note that the SMEI FOV is shifted northward during this season. ACE solar wind data plot shows (e) the magnetic field intensity, the (f) polar and (g) azimuthal IMF components, (h) the solar wind proton temperature (black) and expected proton temperature (red) with the black shading indicating where the proton temperature falls below the expected temperature, (i) the proton density, (j) velocity, (k) helium/proton ratio, (l) the observed and expected O7/O6 ratio, (m) the B_z component of the IMF in GSM coordinates, the (n) *Dst* and (o) *Kp* geoindices, and (p) a 0/1 value indicating whether or not the signatures suggest an ICME flow [e.g., *Richardson and Cane*, 2004]. The vertical red bar indicates the onset time of bright aurora in SMEI (arrow) on 7 and 9 November 2004 when the ICME fronts were at elongations of 105 and 85°, respectively. The second ICME may be more closely associated with the first *Dst* dip (D) before the storm 78 peak. The vertical green lines indicate the ATs of shocks at ACE (see text). ACE plot courtesy of I. Richardson.

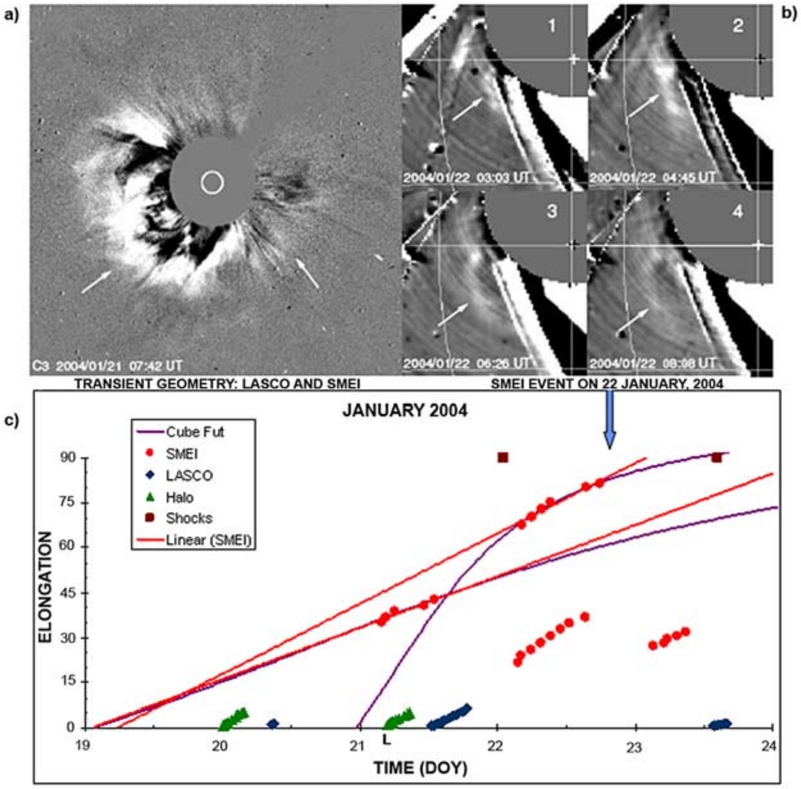

Figure 7. Example of the comparison of ICMEs and ACE shocks from *Howard et al.*'s [2006] study. Event of 21–23 January 2004 (CDAW storm 73). (a) LASCO C3 halo CME, (b) four views of the SMEI transient, and (c) SMEI elongation versus time plot with examples of various fits. These allowed *Howard et al.* [2006] to predict the ICME arrival time and compare it with the actual (shock) arrival time. The arrow indicates the onset time of SMEI aurora.

were first reported by *Johnston et al.* [2004] and discussed by *Howard et al.* [2006] and *Webb et al.* [2006a]. In one study we included all moderate level or greater storms, defined as having a peak $Dst \leq -60$ nT, over an approximately 2-year time period. For 85% (39 of 46) of these storms, SMEI detected a ICME within 2 days prior to the storm onset. Whether all the storms were ICME driven or whether the observed ICMEs could be clearly associated with the subsequent storms was not established, nor were the characteristics of those ICMEs examined.

[24] In another study we examined the sources of only the most intense (peak $Dst \leq -100$ nT) geomagnetic storms during the first 2 years of SMEI observations, from February 2003 to 2005. There were 14 such storms and SMEI had suitable data during 12 of them. For 10 of those 12 storms (83%), SMEI observed associated Earthward-directed ICMEs. During all 12 storms SMEI also observed the bright auroral light associated with the storm. The mean time difference between the first SMEI observation of the ICME and the arrival of the associated shock at Earth was 18.6 hours. The mean difference between the first ICME observation and the storm onset was 29.25 hours.

[25] These two studies were the first to show that SMEI could detect fairly fast Earthward ICMEs from ~10 hours to ~2 days before their Earth arrival and that, given much better data latency, a future SMEI-type heliospheric imager could be used to forecast the onset and maybe even the intensity of geomagnetic storms. These preliminary studies have now been expanded and combined with the identification results of the Geostorm CDAW to cover all intense storms during the SMEI observations from February 2003 to 2007. Those results are the focus of this paper.

3.2. Comparing LASCO CMEs and SMEI ICMEs With ACE Shocks

[26] *Howard et al.* [2006] studied 20 ICMEs observed by SMEI over its first 19 months that were associated with LASCO halo CMEs and shocks observed by ACE at the L1 point. Their study focused on computing distance-time profiles using both the LASCO CME and SMEI ICME data to determine ICME speed, and then to predict its time of arrival at Earth. They used the shock arrival time (AT) at L1 as the indicator for ICME arrival, thus ignoring the shock standoff distance (time) from the ejecta. They then com-

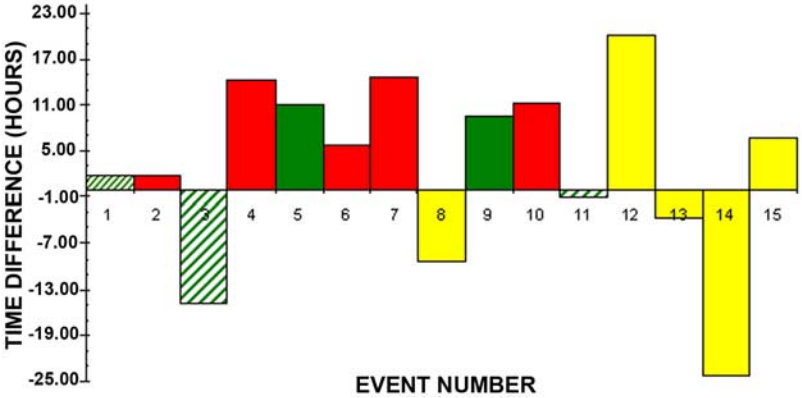

Figure 8. Time difference histogram comparing the predicted (LASCO and SMEI Ejecta) and actual (ACE shock) arrival times (15 events with storms). The colors denote different levels of storms, i.e., green are small, yellow are medium, and red are large storms, respectively. The cross-hatched bars are for storms with no sudden storm commencements (SSCs); see *Howard et al.* [2006] for details. Algebraic mean is +4.0 hours. RMS is 11.4 hours.

pared the predicted ICME AT with the actual shock ATs at ACE at L1.

[27] The angular distance from the Sun traversed by an ICME is typically characterized by its solar elongation angle, ε. In ecliptic coordinates, the center of the Sun is at $\varepsilon = 0°$, ε is the polar distance and position angle (PA) is the associated polar coordinate. For SMEI, the elongation ε of the leading edge of an ICME versus time plot provides the primary information on the outward motion of the ICME. Only angular speeds can be derived from fits to the ε versus time plot for a given ICME. To calculate true speeds, some assumptions or a particular model must be used. *Howard et al.* [2006] computed speeds on the basis of the so-called "point P approximation." This depends on the assumption that the ICME front can be approximated as a Sun-centered circular arc and that the maximum density along the line of sight occurs at the closest approach point of that line of sight to the Sun, i.e., at the tangent point, P, of the arc. The distance from the Sun to P then is equal to the sine of the observed ε, since SMEI is at 1 AU from the Sun, and the speed is the change of this distance with time, converted to appropriate units, such as km/sec. The point P approximation provides only lower limits to the true distances and speeds of ICMEs as viewed by SMEI and is less accurate for ICMEs approaching Earth.

[28] Figure 7 shows an example of one of the 20 *Howard et al.* [2006] events, their event number 15 on 21–22 January 2004. We feature it here because it is also one of the CDAW storm events, number 73, and illustrates the method they used. Figure 7a shows the LASCO halo CME on 21 January, and Figure 7b shows the ICME front traveling through the SMEI field on four sky maps on the next day. Figure 7c shows the elongation-time plot with the LASCO CME and SMEI ICME points and the ACE shock arrival time at 1 AU. A linear fit through the SMEI points on the (point P) distance-time plot (not shown) projects to 2106 UT on 22 January, whereas the actual shock arrival time was at 0105 UT on 22 January. So, in this case, SMEI would have predicted a storm (shock) time ~20 hours too late.

[29] During 2003–2004, 20 shocks were associated with SMEI ICMEs with 15 of these also associated with moderate to strong storms. Using the above technique, *Howard et al.* [2006, Table 3] determined the time differences between the predicted (LASCO CMEs and SMEI ICMEs) and actual (ACE shocks) ATs for these 15 events. Figure 8 is a histogram of these time differences between the predicted and the actual ATs. The algebraic mean for the ICME AT-shock time differences that we calculated from these results was +4.0 hours. In section 4.2.1 we will compare these results with those from our analysis of the CDAW events.

3.3. Space Weather Forecast Model Corrections Using SMEI

[30] SMEI provides important observations of the propagation and evolution of ICMEs which contribute to understanding ICMEs and their interaction with the background solar wind. Timely SMEI observations of ICMEs can improve space situational awareness and solar wind forecast skill. At a fundamental level, SMEI images can confirm or refute whether an ICME that is predicted by a physics-based solar wind model is actually en route to Earth. SMEI data can also enable midcourse updates or corrections to operational solar wind forecasts more than a day or two before the disturbance hits Earth.

[31] Currently, we are investigating the use of SMEI observations to compare with the Hakamada-Akasofu-Fry Version 2 (HAFv2) 3-D solar wind model [*Hakamada and Akasofu*, 1982; *Fry et al.*, 2001, 2003]. The HAFv2 model is a kinematic model that predicts solar wind conditions (speed, density, dynamic pressure, and interplanetary magnetic field) at Earth and elsewhere in the solar system

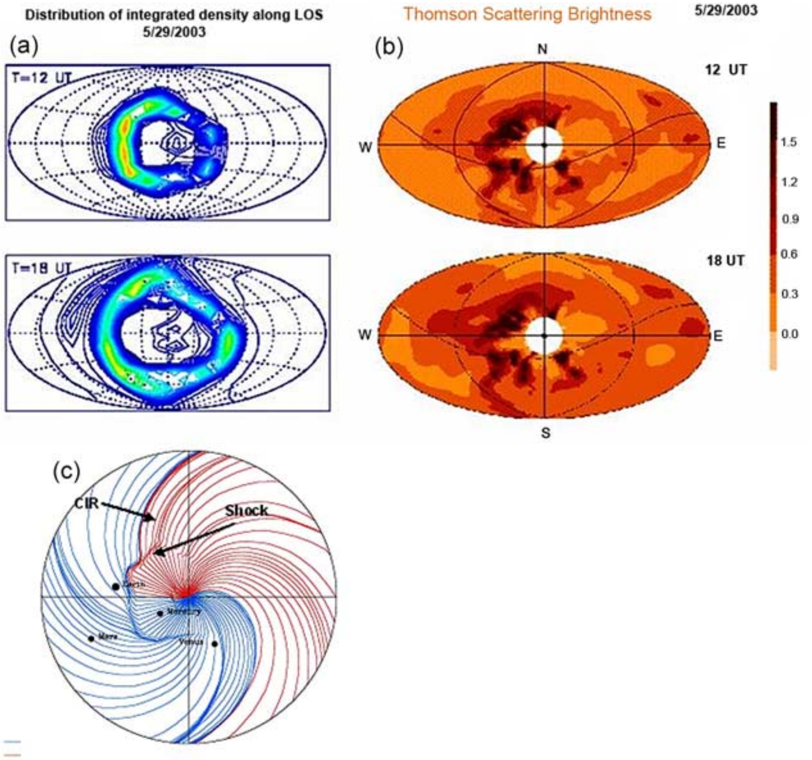

Figure 9. (a and b) Comparison of shock/compressed IP density of HAFv2 model and SMEI observations for the 29 May 2003 halo ICME (Figure 1), associated with CDAW storm 63; (c) HAFv2 forecast of ecliptic plane IMF showing the shock propagating through a preexisting corotating interaction region (CIR). The reconstructed HAF density maps suggest that the transient viewed by SMEI is brighter to the east because of the added contribution from the CIR. After *Sun et al.* [2008].

based on observations at the Sun. These solar wind parameters are key inputs to numerical prediction models for forecasting space weather disturbances that impact space operations. The HAFv2 model is a single-fluid, Parker-like, modified kinematic model that projects fluid parcels outward from the rotating Sun along fixed radials at successive time steps, in an inertial frame. The parcels move outward with different speeds along fixed radials as the Sun rotates beneath the radial grid. The frozen field condition mandates that, along each radial, the faster parcels do not move through or pass slower parcels. Therefore, the kinematic flow is modified, in that the fluid parcel positions are adjusted to account for the stream-stream interaction as fast parcels (solar wind streams) overtake slower ones. The model has been calibrated so that HAFv2 output matches a 1-D MHD solution. If the speed gradient along a radial is steep enough, corotating interactions and interplanetary shocks are formed.

[32] The HAFv2 model uses two sets of inputs. The first set establishes the steady state boundary conditions for the ‘‘quiet,’’ or background solar wind, and the second set determines the time-dependent boundary conditions for the event-driven solar wind. The HAFv2 model uses source surface maps derived from synoptic solar observations [*Arge and Pizzo*, 2000; *Arge et al.*, 2004] to establish the background solar wind conditions. It is also driven by proxies for energy released during solar events to model CMEs and interplanetary shock propagation. The HAFv2 model maps the disturbed and the undisturbed solar wind, so it is applicable to all phases of the solar cycle. In addition, HAFv2 produces chronological sequences of the ecliptic plane interplanetary magnetic field (IMF) and other solar wind parameters.

[33] We are using HAFv2 to compute time-dependent solar wind density maps at times corresponding to SMEI image frames. We compute synthetic skymaps of Thomson-scattering brightness by integrating heliospheric density along lines of sight centered at Earth, with the Sun at the center. Total brightness was computed using algorithms provided by one of us (BVJ [see also *Jackson et al.*, 2006; *Billings*, 1966]), using a technique developed by *Sun et al.* [2008]. The result is a series of sky plane, Aitoff-projected images of the modeled ICME taken at the appropriate time. These were converted into files in the same FITS format as those from SMEI, so that measurements of predicted ICME morphology and propagation can be obtained in the same manner using the SMEI analysis software.

[34] Specific studies have been done comparing SMEI and HAFv2 for events in February 2003 and February 2004 [*Howard et al.*, 2007], and for the 28–29 May 2003 event [*Sun et al.*, 2008]. Figure 9 illustrates this comparison for the latter event. *Jackson et al.* [2008] describe a 3-D reconstruction of this event using the most recent UCSD-processed SMEI data and comparisons with the LASCO CMEs, the HAF model, and ACE in situ data. In these studies the SMEI images have confirmed that the HAFv2 simulations of the ICME geometry are reasonably accurate. However, in the two events of *Howard et al.*'s [2007] paper and in subsequent studies, it has been demonstrated that the HAFv2 model's synthetic skymap calculation overestimated the ICME speed as measured by SMEI by about a factor of 2. Thus, the SMEI data has already helped to find and correct an error in the calculations in a space weather model. (Note that this error is not present in the shock arrival time forecast component of HAFv2 used in the "Fearless forecast" studies described below.)

[35] One goal is to improve the operational solar wind forecasts at the Air Force Weather Agency (AFWA) that are based upon a version of the HAFv2 model which became operational in August 2006. The technical objective is to determine a set of procedures that the duty forecaster can use to update or correct a solar wind forecast using heliospheric imager data such as from SMEI. The following scenario describes how this forecast adjustment might be done in an operational environment.

[36] We assume that the forecaster has access to a SMEI point-and-click analysis tool and that timely SMEI images are available for analyses. When a solar event occurs, the forecaster will run the HAFv2 model to make an ICME/shock prediction. The HAFv2 model also produces synthetic skymaps of predicted ICME brightness for comparison with SMEI images. The forecaster will use SMEI imagery to observe and track the ICME. The forecaster will measure the ICME location and speed using the SMEI imagery and using the synthetic skymaps produced by HAFv2. Comparing the SMEI-based and HAFv2-based results, the forecaster will adjust a key input to HAFv2, such as the initial speed of the disturbance at the Sun. The forecaster will rerun HAFv2, iterating until the observed and forecast skymaps match. The final HAFv2 solution becomes the new forecast. When the ICME/shock arrives at (or does not reach) Earth, the forecaster verifies the forecast and updates the forecast skill statistics.

[37] Another approach for comparing the forecasting capabilities of the HAF model and SMEI observations involved comparing real-time "Fearless Forecasts" of shock arrival time [*Fry et al.*, 2001, 2003] with retrospective SMEI-based forecasts for the 20 "halo" ICME events given by *Howard et al.*'s [2006] study, and computing the resultant forecast skill scores [see *Fry et al.*, 2006; *Webb et al.*, 2006b]. An earlier study of HAFv2 forecasts of shock arrival times (SATs) during 1997–2002 showed only a moderate success rate (number of correct forecasts/total forecasts) >50%. *Howard et al.* [2006] compared SMEI ICMEs associated with LASCO halo CMEs and ACE shocks at L1 over a 1.5-year period. *Fry et al.* [2006] determined the forecast hits, misses, false alarms and correct nulls for *Howard et al.*'s [2006] ICMEs (ex post facto forecasts), and compared these with the corresponding real-time forecasts by HAFv2. For our purpose a Hit = shock predicted within ±24 hours of observed; a Miss = shock observed but not predicted; a False Alarm = shock predicted but not observed; and a Correct Null = shock correctly predicted to not reach Earth.

Table 1. Contingency Table for SMEI Versus HAFv2 Forecasts

ACE L1 Observation	Forecast		SMEI-Based Forecast		HAFv2 Forecast	
	Yes	No	Yes	No	Yes	No
Yes	hit	miss	14	0	6	8
No	false alarm	correct null	6	0	0	0
Total			20	0	6	8

[38] From these results they formed a 2 × 2 contingency table, updated as shown in Table 1. For the 14 geomagnetic storms associated with the 20 "halo" ICMEs given by *Howard et al.* [2006, Table 3], we issued 8 "Fearless Forecasts" of SAT. Six of these forecasts were hits and two were misses (i.e., predicted SAT minus observed SAT outside the ±24-hour window). For 6 of the storms where SMEI observed ICMEs en route, FFs were not issued because the information for the solar events did not meet our criteria for running the model and issuing a forecast (as defined by *Fry et al.* [2003]). Had we initiated forecasts based upon the SMEI observations, 6 additional forecasts would have been possible. These forecasts can also be considered misses, bringing the total to 8 misses and 6 hits. Thus, for this period near-real-time SMEI observations, if available, could have nearly doubled the HAFv2 forecast rate (i.e., the 6 additional new shock forecasts versus the 6 hits + 2 misses).

[39] Models such as the HAFv2 model simulations of the 28–29 May 2003 event can also be used to help explain unexpected features in the SMEI observations. In *Sun et al.*'s [2008] simulations of this event, they showed why this halo ICME (Figure 1) appeared brighter to the east when the flare associated with the CME and the assumed location of the HAF energy origin was west of Sun center. The reason was that a preexisting corotating interaction region (CIR) likely contributed to the density integrated along the line of sight through the eastern part of expanding ICME front, increasing the brightness of that part of the "halo" (Figure 9).

[40] To summarize this section, we have found that heliospheric imagers such as SMEI can enable significant improvements in operational space weather forecasting skill. Specifically we compared forecasts made with the HAFv2 model with corresponding SMEI imagery. We found that SMEI observations of ICMEs, if available in near-real time, can be used to make midcourse corrections to the HAFv2 model forecasts. We presented one concept of operations for adjusting the HAFv2 forecast based upon SMEI data. SMEI observations and HAFv2 simulations are

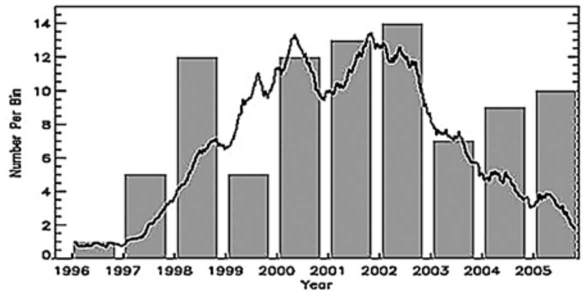

Figure 10. The yearly occurrence rate of the 88 CDAW storms. The black curve is the 180-day running average of daily sunspot numbers in arbitrary units. From *Zhang et al.* [2007a, 2007b].

complementary in that combining them improves both the accuracy of the HAFv2 model-based forecasts and the interpretation of the SMEI observations.

4. Comparing SMEI ICMEs With the CDAW Intense Storms

4.1. Data and Statistical Analysis

[41] Here we describe the comparison of the SMEI ICME observations with the intense geomagnetic storms that were the focus of the NASA LWS Geostorm CDAW. CDAW WG1 studied all major geomagnetic storms of cycle 23 that occurred between January 1996 and December 2005. We summarize the method of selection of the storms as discussed by *Zhang et al.* [2007a]. This 10-year period extends from the start to late in the declining phase of solar cycle 23, which had two sunspot maxima in 2000 and 2001 (Figure 10). The *Dst* index is a measure of the strength of the ring current and is widely used for measuring the intensity of geomagnetic storms. A major geomagnetic storm was defined as a minimum in the hourly *Dst* index falling below $Dst \leq -100$ nT, a commonly used threshold for major/intense storms [e.g., *Tsurutani and Gonzales*, 1997; *Loewe and Prolss*, 1997]. If a period of high activity showed multiple $Dst \leq -100$ nT minima, CDAW WG1 arbitrarily assigned these to a single storm event if the minima were separated by less than 24 hours, rather than define each minimum as a separate storm. CDAW WG1 identified 88 major geomagnetic storms during this 10-year period, using these selection criteria. These storms are listed by *Zhang et al.* [2007a, Table 1], which was corrected by *Zhang et al.* [2007b].

[42] Since initiating operations in February 2003, SMEI was able to observe the associated ICMEs for most of the CDAW intense storms. Here we describe the SMEI observations and analyses for the 26 CDAW storms, CDAW numbers 63–88, that occurred during the SMEI observations from May 2003 to October 2005. In addition for completeness, we include the two other intense storms that occurred after that period through the end of 2007 for a total of 28 storms. The solar and IP drivers of these latter storms were unambiguous.

[43] These 28 storms are listed in Table 2, along with details of the SMEI observations and of the CDAW-identified solar and interplanetary (at 1 AU) sources of the storms. Details of the search and identification process are given by *Zhang et al.* [2007a] and will not be repeated here. For our study we assume that these identifications were correctly made and we will use the timing and location information as given by *Zhang et al.* [2007a, Table 1]. We merely note that the identification procedure used by CDAW WG 1 focused on identifying the chain of activity preceding a storm starting with the solar CME and associated surface activity and then the interplanetary counterparts of this ICME at 1 AU, especially considering evidence of shocks, magnetic clouds and other ICME material. The primary data sets used were from the SOHO LASCO coronagraphs and EIT instrument at the Sun, and from the ACE spacecraft at L1 and the Wind spacecraft near Earth. In addition, we note that the SMEI observations discussed herein were used by the working group to help track ICMEs to larger distances from the Sun than is possible with LASCO and, therefore, to aid in the identification and timing of the Earth arrival of the shock and/or ICME, and the storm onset.

[44] Table 2 presents the basic data and some results for our study of SMEI's observations of ICMEs associated with the CDAW storms. The first three columns of Table 2 give for each storm its CDAW number, the peak intensity in −*Dst*, and its estimated onset (first row) and peak (next row) times. The *Dst* data were obtained using the Kyoto geomagnetic data at http://swdcdb.kugi.kyoto-u.ac.jp/dstdir/index.html. The storm values through 2003 were based on the final *Dst* index, whereas those in 2004 and 2005 were based on the provisional *Dst* index, so that the final values may change slightly. We estimated onset times from the hourly index based on the hour when *Dst* began a systematic drop starting at ~ -40 nT until it reached its minimum intensity. The next eight columns describe the SMEI data for each ICME that we associated with each storm. The last nine columns are from the CDAW Table 1 and describe the properties of the solar source(s) and the properties of the IP source(s) that the CDAW working group decided directly "drove" the geomagnetic activity.

[45] For the SMEI data, in Table 2, in the Time First Observed column two dates (and day of year) and times are given when SMEI first observed the ICME (top) and the estimated time (hour) when it left the Sun (next row). This "onset" time uses a linear extrapolation of data points on an ε versus time plot back to 0 elongation, i.e., the Sun. The Storm/CME Association column indicates whether or not we considered the SMEI transient to be associated with the storm (top) and/or with the LASCO CME(s) (next row) in the Solar column. In the Aurora Date column we give the date and time when SMEI first observed auroral light associated with the storm. In Table 2 the t_{diff} Au-FO column gives the time difference in hours between the ICME first observed ("FO") time and the auroral ("Au") onset

Table 2 (Sample). CDAW Storms and SMEI CMEs[a] [The full Table 2 is available in the HTML version of this article]

CDAW Storm	Storm Intenstiy (−*Dst*)	*Dst* Date and Time Onset/Peak (UT)	SMEI Time First Observation/ Estimated Onset Date and Time[b] (UT)	Storm/CME Association[c]	Aurora Date and Time (UT)	Predicted 3-D 1AU Arrival Date and Time (UT)	t_{diff} St-Au (hours)	t_{diff} Au-FO St-FO (hours)	Span (degrees)	Elongation at Storm (degrees)
				2003						
63	144	29 May, 2200	28 May (148), 1653	Y	29 May, 1500	29 May, 2134	7.00	22	180	80
		30 May, 0000	28 May, 0500 and 1600	Y		29 May, 2238		29		
64	141	18 Jun., 0700	14 Jun. (165), 1036	N?/N?	Y?	xxx	xxx	xxx	[60	80]
		18 Jun., 1000	13 Jun., 0000	Too early?	(14 Jun., 1217)					
65	*105*	*11 Jul., 0900*	*10 Jul. (191), 0616*	*Y?*	*11 Jul., 0747*		*1.20*	*26*	*80*	*70*
		12 Jul., 0600	*12 Jul., 0443* *8 Jul., 1000*	*Can't tell*				*27*		
66	148	17 Aug., 2300	17 Aug. (229), 0504	Y?	18 Aug., 0130	18 Aug., 0705	−2.50	20.5	60	70
		18 Aug., 1600	14 Aug., 0800	Y?				18		
67	353	29 Oct., 1500	28 Oct. (301), 1303	Y	29 Nov., 1104	29 Oct., 1214	3.90	22	90	70
		30 Oct., 0100	28 Oct., 1100 No data 30 Oct.	Y		~29 Oct., 2000		26		
68	383	30 Oct., 1900	31 Oct. (304), 0527	xxx	31 Oct., 0527	xxx	?	xxx	30	?
		30 Oct., 2300	30 Oct., 0600 Poor data	?				xxx		
69	472	20 Nov., 1100	19 Nov. (323), 0548	Y	<20 Nov., 1040	19 Nov., 1939	?	<29	60	90?
		20 Nov., 2100	18 Nov., 1200	Y	20 Nov., poor	20 Nov., 1836		29		
				2004						
70	149	22 Jan., 1200	21 Jan. (021), 0348	Y	22 Jan., 0535	~22 Jan., 0100	6.40	25.5	30	80
		22 Jan., 1400	~19 Jan., 1200–2000 and 0400 (22 Jan. (022), 0331)	Y?		(22 Jan., 1706)		32		
71	*109*	*11 Feb., 1500*	*(9 Feb. (040), 2054)*	*?*	*11 Feb.,1319*		*1.70*	*40*	*45*	*85*
		11 Feb., 1800		*No CDAW CME*				*42*		
72	112	3 Apr., 1800	(1 Apr. (092), 0942)	Y	3 Apr., 1823	2 Apr., 1634	−0.60	28	45	~70
		4 Apr., 0100	2 Apr. (093), 1359 ~1 Apr. 0000	Y?		3 Apr., 0910 3 Apr., 2339 4 Apr., 0445		28		
73	101	22 Jul., 2300	[20 Jul. (202), 2128]	Y	22 Jul., 1500	22 Jul., 1732	8.00	23	120	70
		23 Jul., 0300	21 Jul. (203), 1602 20 Jul., 1500	Y		22 Jul., 2251		31		
74	148	25 Jul., 0100	Check	N?	Y		xxx	xxx	xxx	xxx
		25 Jul., 1200		?	Aurora continues from above					

[a] Italicized values were not used in this study. Parentheses or brackets around entries indicate uncertain data or associations except for the SMEI time first observation/estimated onset date and time information. Here xxx means that there is no data available.

[b] Numbers in parentheses are the day of year.

[c] Y, yes; N, no.

[d] F, flare; FH, halo.

(top) and storm (''St'') onset (next row) times. Finally, we give the estimated span of the ICME and its estimated elongation at the time of storm onset, both in degrees. These data and results will be discussed later. The Predicted 3-D and t_{diff} St-Au columns are also discussed later.

[46] In Table 2, in the Solar column is listed the solar source type as S, single CME (18 events); M, multiple CMEs (6); and CH, coronal hole (4). Considering the properties of solar sources, the Onset Date and Time column gives the first appearance of the CME in the LASCO C2 coronagraph, the CME Speed column gives the average speed of the CME through a linear fit in the LASCO C2/C3 fields of view, and the Width column gives the apparent angular span of the CME in the plane of the sky measured in the C2 field of view. These values were generally obtained from the online LASCO CME catalog at http://cdaw.gsfc.nasa.gov/CME_list/ [*Yashiro et al.*, 2004]. Source Location column gives the heliographic coordinates of the associated surface activity. This generally corresponds to the Hα flare location reported by the NOAA Space Weather Prediction Center (SWPC). When no Hα flare location was reported, SOHO EIT images were used to measure the source coordinates, given by the location of any brightening or the dimming regions observed. The surface identification of the candidate CME for storm 76 was considered inconclusive, however we did not consider that storm because of poor SMEI data. Because of SOHO data gaps, the solar source for storm 72 was identified with a major long-duration solar flare in the GOES SXI imager and a halo CME observed a few hours later in LASCO C3.

[47] In Table 2, for the 6 M-type events, numbers 63, 64, 77, 78, 79, 86, there are multiple rows for each event listing the multiple CMEs that may have contributed to the observed 1 AU solar wind structures. In each case, the first row indicates what is considered the ''principal'' solar driver. In the case of the 4 C-type events, the definitions of the parameters in the solar source columns are slightly different because of the different nature of the source. The time in the Onset column is the central meridian transit time of the centroid of the associated coronal hole measured from EIT images. The time is followed by ''(CH)'' in order to emphasize that this does not refer to a CME source. The data for the storms driven by CH-CIRs, numbers 65, 71, 81, 87, are italicized; these events were not used in this study.

[48] For the properties of the IP sources, in Table 2, the IP column summarizes the solar wind components at 1 AU, in time order, that CDAW WG1 identified as driving the storm. The primary drivers were considered to be periods of southward magnetic field either in shock-related material or in the ICME. The structures in IP are SH, shock sheath; ICME, interplanetary CME; MC, magnetic cloud. (M) indicates multiple structures of that type. A hyphen indicates an interaction between two structures, in particular, preceding ICME (PICME)-SH (numbers 64 and 78) denotes a shock propagating through a preceding ICME. The Shock and ICME Onset columns show the date and time of the ICME-driven shock from ACE or Wind and the onset time of the ICME, respectively. For number 64 the first row is an estimate for the shock arrival time. The t_{diff} Au-Sh column will be discussed later.

[49] Next we discuss several examples illustrating the SMEI geoeffective ICME observations and how they related to solar wind conditions in front of Earth and the storm effects at Earth. The first example was introduced earlier. This was the first Earth-directed ICME detected and analyzed in the SMEI data, occurring on 28–29 May 2003, 5 months after observations began [*Tappin et al.*, 2004; *Jackson et al.*, 2007] (Figures 1–3). This fast (1000 km/s) event was detected at $\sim 30^\circ\ \varepsilon$, about 15 hours before it passed over the Earth on 29–30 May 2003, causing a major geomagnetic storm. The ICME erupted from the Sun following two bright (X-class) flares from an active region near Sun center. These yielded two nearly simultaneous halo CMEs in LASCO which SMEI later saw as three contiguous arcs together covering over 150° of sky (Figure 1b).

[50] The elongation-time plot of the leading edges of the LASCO CME and SMEI ICME features are shown in Figure 2 (top), along with time markers at $90^\circ\ \varepsilon$ indicative of the ATs at 1 AU (from Table 2) of solar wind shocks (asterisks), the SMEI aurora onset time (crosses), and the storm onset and peak times (the two bars, respectively). The bottom plot is in ''distance'' versus time wherein we converted the LASCO CME and SMEI ICME ε-time data by assuming that the CME was launched from the CDAW-identified source location and propagated radially from the Sun. This method is discussed later in section 4.2.1. Here the time markers are accurately located at 1 AU. These data were then used to calculate the arrival times of the ICME structures at 1 AU based on linear fit extrapolations of the 3 separately tracked SMEI features (the two later ATs are given in the Predicted 3-D column of Table 2). This shows that two of the SMEI features might have been associated with the two shocks, with the SMEI aurora onset time lying between them. The third, and best observed SMEI arc was closely associated with the storm onset itself. This timing is confirmed in the solar wind and geomagnetic data plot of Figure 3. Key solar wind plasma, composition and IMF parameters are shown in these plots (see also Figures 5f–5p and 12) as well as the *Dst* and *Kp* geoindices. The vertical red line denotes the SMEI aurora onset time between the two shocks, and about 7 hours before the *Dst* storm onset (however, note that the 3-hour *Kp* index is enhanced earlier). CDAW WG1 determined that this storm was caused by southward IMF mostly between the two shocks, with multiple and compressed ICME material involved. There was clear ICME material and strong IMF following the second

shock but the IMF was strongly northward, minimizing any coupling.

[51] During two weeks in late October and early November 2003, a series of large solar events led to high levels of energetic particles in geospace and produced overlapping large geomagnetic storms on 28–30 October. Eruptions came from three active sunspot regions. The first rotated into view on 19 October and over the next two weeks the three regions unleashed 11 major, X class flares, an unprecedented production rate for such powerful events. The three most geoeffective flares and halo CMEs occurred on 22, 28, and 29 October. The weaker 22 October ICME caused only a brief geomagnetic storm that was terminated by strong northward fields within the ICME. However, the 28 and 29 October flares had peak fluxes as measured by the NOAA GOES satellites (X17 and X10) that were among the largest ever recorded, and were associated with large particle events at Earth peaking early and late, respectively, on 29 October. The shock waves from these events arrived at Earth only 19 hours after leaving the Sun, among the fastest events ever observed since the dawn of the satellite age [*Cliver et al.*, 1990]. These shocks and their trailing ICMEs drove two intense storms, CDAW storms 67 and 68, with peak *Dst* values both on 30 October of 353 and 383 nT, respectively.

[52] SMEI observed the 22 and 28 October halo ICME events, again starting at distances about 1/3 of the way from the Sun to Earth and 21 and 10 hours, respectively, before Earth arrival. However, the second energetic event, on 29–30 October, was one of the 7 CDAW storms for which SMEI had no or insufficient data. This was because the intense particle bombardment and aurora from the first SEP event and storm knocked out the instrument through most of 30 October and into 31 October! For the 28–29 October storm (67, plot not shown), SMEI observed two ICME arcs; the d–t plot yielded ICME ATs at 1 AU between the shock AT and storm onset and after storm onset, respectively (Appendix A).

[53] Figures 5 and 6 show SMEI and solar wind data during the period in November 2004 involving the two CDAW storms 77 and 78. The solar wind plot in Figure 5 shows that, although there were a number of shocks during this 4–5 day period, there were clearly two long ICME intervals (Figure 5o) associated with the strong, southward IMF driving the storms. These intervals are denoted by magnetic clouds (Figures 5e–5g), low Tp and density (Figures 5h and 5i), and high He and O7/O6 content (Figures 5k and 5l). The storms were driven (1) in CDAW 77 by high speed and southward fields associated with multiple shocks and the first cloud and (2) in CDAW 78 a shock propagating through this preceding ICME (note the *Dst* dip labeled 'D') followed by another shock and the second cloud. SMEI observed at least two large arcs or partial halos east and southeast of the Sun from 5 to 7 November that may have merged near Earth (Figures 5a–5c). Two fainter arcs were seen off the west limb on 8–9 November (Figure 5d) that were possibly associated with dip D and/or storm 78. The vertical red bars on Figures 5e–5o indicate the times when the aurora associated with the two storms were first observed by SMEI. The ICME arcs leading edges were at 105° and 85° ε, respectively, at these times that were each about half a day before the storms' main phases. This shows the lead times that a SMEI-type imager could provide.

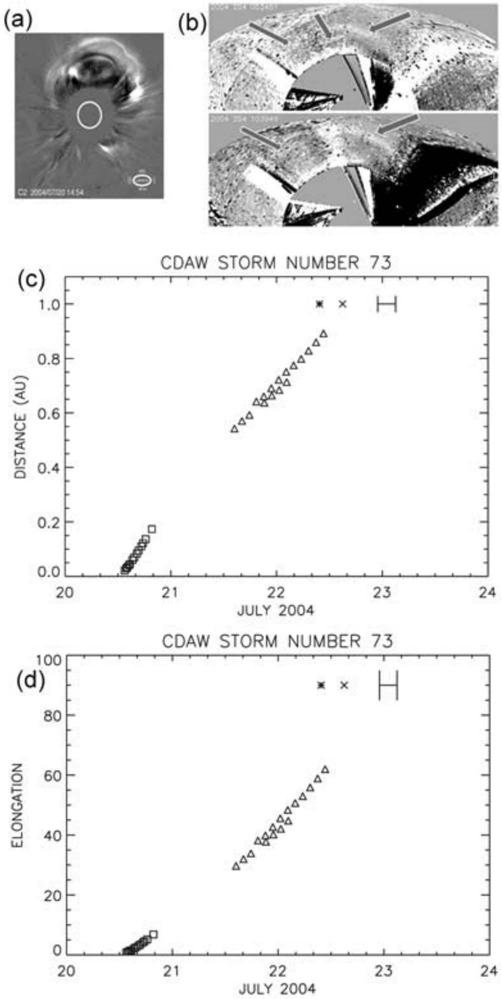

Figure 11. Example of an Earthward partial halo ICME/ICME and CDAW storm 73. (a) LASCO C2 difference image on 20 July 2004 at 1454 UT. (b) SMEI difference images on 22 July at 0530 and 1040 UT showing the halo structures (arrows). The storm onset was on 22 July at ~1500 UT (Figure 8). (c) Distance-time plot and (d) elongation-time plot. Symbols are as in Figure 2.

[54] Figure 6 shows the e–t and d–t plots for this period, with the LASCO CME and SMEI ICME fronts and the time markers at 1 AU. Both plots show the 1 AU AT of the first ICME between the first shock AT and the SMEI aurora onset time, and the second ICME AT coincident with another shock and several hours before the *Dst* dip, D, that preceded storm 78. Thus, the second SMEI ICME

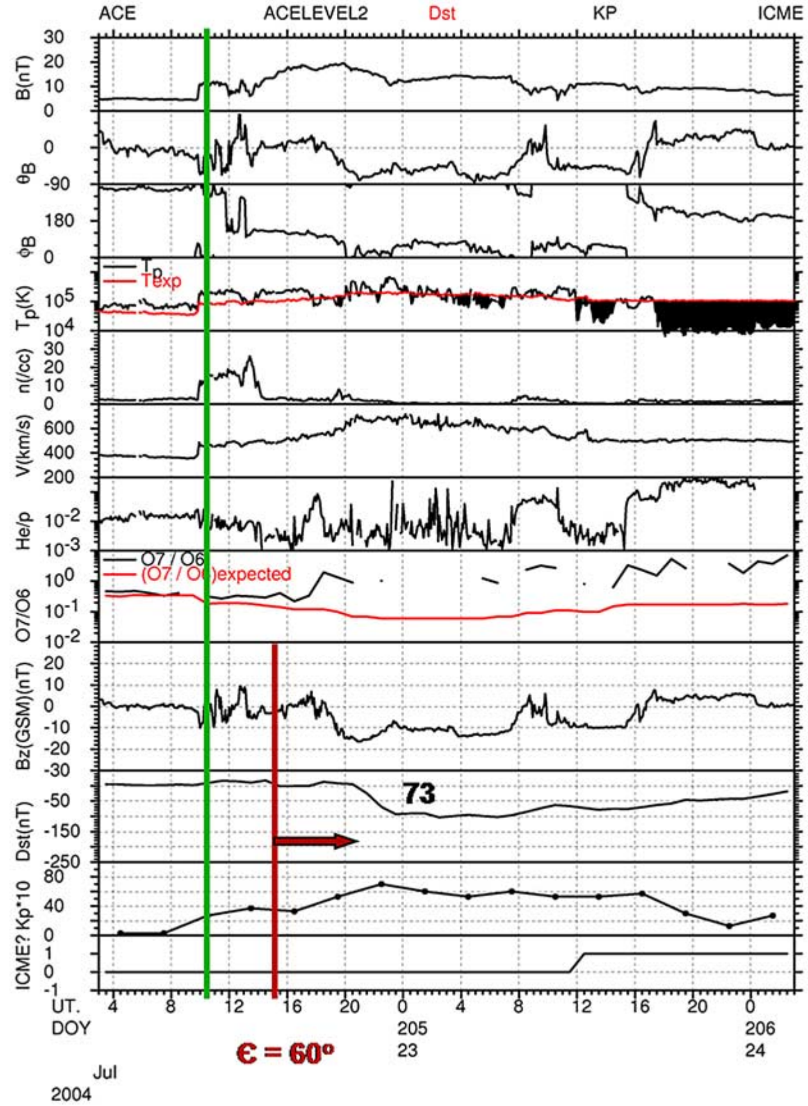

Figure 12. ACE solar wind and storm data for 22 – 23 July 2004 ICME and CDAW storm 73. Plot is as in Figure 3. The vertical red bar indicates the onset time of bright aurora in SMEI (arrow) when the ICME front was at an elongation of 60°. The vertical green line indicates the shock AT at ACE (see text). ACE plot courtesy of I. Richardson.

may have been associated with this dip. Although of short duration, this dip was still significant (peak = 223 nT) and likely driven by the compression due to the second shock and ICME running into the first.

[55] Our final example involves CDAW storm 73 in July 2004. A large-scale eruption occurred over the northwest part of the Sun on 20 July leading to a partial halo CME in LASCO over the entire northern hemisphere (Figure 11a). Later, on 21 – 22 July SMEI observed the ICME as several expanding arcs covering the northern ecliptic hemisphere reaching spans of 120° (Figure 11c). The $d-t$ plot of Figure 11c shows how well the LASCO and SMEI points line up for this event, and that the SMEI predicted AT at 1 AU is nearly simultaneous with the SMEI aurora onset time at 22 July at 1500 UT. This time is also about 7 hours between the shock AT and storm onset (see the solar wind data for this event in Figure 12), illustrating the general pattern found for all the CDAW storms (see below). CDAW WG1 concluded that the storm was driven by southward field and high speeds in the ICME following the shock and its sheath region.

[56] Next we provide some statistical results derived from the tabular data. Figure 10 presents the annual occurrence rate of the 88 intense CDAW storms with sunspot numbers superposed on it. We see that the storm rate peaks with the sunspot numbers in 2000 – 2001, but that there are many storms during the rise and declining phases of the solar cycle. The storms of this study include those in the last 3 bins, 2003 – 2005 plus the two additional events through

2007, all occurring during the declining phase of this cycle. Of the 28 intense storms during this period, 7 have either no or inadequate SMEI data coverage preceding the storm peak, leaving 21 events for further study. Three of these 21 storms were identified during the CDAW as being driven solely by CIRs associated with solar coronal holes (numbers 65, 71, 87). The CIR-driven CDAW storms were discussed by *Richardson et al.* [2006]. Since it has not yet been demonstrated that SMEI can detect CIRs, we will not consider these storms.

[57] This leaves 18 remaining storms with adequate SMEI coverage and for which CDAW WG1 identified the solar and IP sources. Of these 18 storms, 12 were preceded by a definitely associated SMEI ICME, 4 by a likely associated ICME and 2 had no associated ICME. Thus, we can conclude that for 89% (16/18) of the intense storms during this period, SMEI likely detected and tracked the ICMEs that caused the storms.

[58] The storm-SMEI ICME associations were done independently of knowledge of the solar and IP sources. Thus, we can evaluate whether or how well the 16 SMEI ICMEs associated with the storms could be identified with the CDAW-source CMEs. In these 16 cases, the SMEI ICMEs and LASCO CMEs were definitely associated in 9 cases, likely associated in 5, and questionable in 2. Thus, in 87.5% (14/16) of the storm-SMEI ICME events, SMEI likely detected the geoeffective ICME observed by LASCO leaving the Sun. On the other hand, since all the storms had reasonably reliable solar CME identifications, this suggests that SMEI did not clearly detect the appropriate ICME in 4 cases, the two questionable cases (numbers 85 and 86) and the two other cases with no SMEI ICME (numbers 64 and 74). However, in event 85 CDAW WG1 concluded that the solar source was inconclusive, and there were either SOHO or SMEI data gaps during the other events. Thus, even in some or all of these 4 ''no detection'' cases, SMEI might have detected the geoeffective ICME given full coverage.

[59] As discussed earlier, one of the unexpected discoveries of SMEI is that it is able to detect auroral light above its orbital height during geoactivity periods when $Kp > \sim 4$ [*Mizuno et al.*, 2005]. The intense storms considered here typically reach higher levels of Kp, and the $Kp = 4$ level corresponds to the $Dst = -40$ nT level we used to define the onset of each storm [*Loewe and Prolss*, 1997]. Thus, the SMEI sky maps could readily be used to determine the onset time of each of the CDAW storms, even in those cases where SMEI did not detect the oncoming ICME, or there was a CIR source. In the t_{diff} St-AU column of Table 2 we show for each storm the time difference in hours between when the auroral light associated with the storm first appeared on the SMEI sky maps and the storm onset time defined above. Excluding lower limits, the mean of the algebraic differences is +4.1 hours (10 events; range = -2.5 to +8.15 hours). Historically storm sudden commencements (SSCs) tend to precede the main phase of storms. Since SSCs are associated with shock waves in the solar wind, it is of interest to compare the timing between the CDAW shock times observed by either ACE or Wind and the onset time of the SMEI aurora. So, in the Shock column we list the time difference in hours between when SMEI first observed the aurora and the 1 AU shock time. Excluding lower limits, the mean of the algebraic differences is +3.9 hours (14 events; range = -22.9 to +15.4 hours). Thus, on average the shock arrived ~4 hours before the SMEI auroral onset, which in turn preceded the storm onset by ~4 hours. These time differences probably have uncertainties of 1–2 hours, because SMEI's time resolution is dictated by its 102-min orbit and Dst is a 1-hour averaged index. We have also not corrected for the time a shock takes to travel the distance between the L1 point where ACE is and Earth. For typical solar wind speeds this travel time is approximately 40 min.

[60] Thus, the typical pattern for these intense events was (1) arrival of the IP shock followed ~4 hours later by (2) the SMEI auroral onset followed ~4 hours later by (3) the storm onset ($Dst \leq -40$ nT criterion). We can think of two reasons why the SMEI aurora precedes storm onset by a few hours. First, it is known that IP shock-driven SSCs usually are associated with a sudden brightening of the aurora [*Craven et al.*, 1985; *Egeland et al.*, 1994; W. Burke, private communication, 2008]. Second, this suggests that SMEI may be sensitive to even lower auroral light levels than the $Dst \leq -40$ nT level, and, therefore, might begin to detect the aurora before the -40 nT level is reached. Of course, the Dst index is defined from low-latitude geomagnetic observatories that sample effects in the ring current at altitudes of several hundred km. Since SMEI views light emission above heights of a few thousand km, it is seems remarkable that the correspondence with the Dst index is so good.

[61] In Table 2, in the t_{diff} Au-FO column (top row) we show the time difference between when SMEI first observed the ICME and when the SMEI aurora first appeared. The next row of the t_{diff} Au-FO column gives the time difference between the SMEI ICME first observed time and the storm onset time. The means of these two time differences are 23.2 hours (11 events; range = 7–36 hours) and 27.5 hours (15 events; range = 14–44 hours), respectively. (The difference in these two mean values, of course, is the 4-hour average difference discussed above between the SMEI aurora and storm onset times.) From a space weather standpoint, the most important conclusion from these timing studies is that SMEI could detect and begin to track the geoeffective ICME an average of 28 hours before it ''struck'' Earth, in terms of the Dst-defined storm onset. Thus, this represents an average lead time or warning time for a storm which could be provided by a similarly designed heliospheric imager with real-time data latency capability. Since the average transit time of the ICMEs (storm onset – CME onset) was 54 hours, this suggests that SMEI could begin to track them halfway between the Sun and Earth. The range in this warning time was 0.6–1.8 days, depending on such factors as ICME speed, brightness, data coverage, etc. (the range of ICME transit times was 1.15–3.2 days).

[62] In Table 2, the Span column shows the estimated maximum angular span in degrees of the geoeffective ICME structure observed by SMEI. The angular span is the difference in Position Angle between the observed sides of the ICME structure. This is often a lower limit because of interference by particles, auroral light, and saturated or shutter-closed frames. The mean span of 78.6° (11 events; range = 30–130°) is typical, or slightly larger than those of the Earthward, arc-like events discussed in section 2.2. This large size is not unexpected for a plasma cloud that is observed as it is traveling near the Earth.

[63] In Table 2, the Elongation column gives the estimated elongation of the leading edge of the ICME observed by SMEI at the time of storm onset. The mean ε = 78.7° (15 events; range = 45–105°). Calculations suggest that such large elongation values are expected for solar transients traveling to 1 AU and beyond and to within the Earth's vicinity [e.g., *Kahler and Webb*, 2007]. However, for events directed Earthward, the observations are complicated by the varying geometry and size of the ICME as well as by its brightness which is affected by Thomson scattering [*Vourlidas and Howard*, 2006]. That the geoeffective ICMEs have both large spans and large elongations at storm onset does not necessarily tell us much about their inherent size or geometry, only that they are being viewed nearby, i.e., when close to Earth. Their arc-like nature suggests that we are viewing the emission across a spherical surface but we do not know whether the true "nose," or radial center of curvature, is along that surface. See the appendix of *Kahler and Webb* [2007] for a discussion of geometry versus distance measurements of ICMEs.

4.2. Forecasting Implications of the SMEI Results

4.2.1. Using SMEI Data to Predict Geoeffective ICME Arrival Times

[64] We can now use the results of the SMEI-CDAW study to update and extend *Howard et al.*'s [2006] result discussed in section 3.2, specifically to produce a new version of the time difference results that we produced from their data (Figure 8). Their study compared SMEI ICMEs associated with LASCO halo CMEs and ACE shocks at L1 over a 1.5-year period. Our study began with the CDAW storms and their identified CMEs and source regions and searched for associated SMEI ICMEs from 2003 to 2005 (2007). Despite these differences there is an overlap of 8 events between the two studies (CDAW 63, 64, 66, 67, 69, 70, 72, and 73). *Howard et al.* [2006] computed distance-time profiles using the point P approximation to fit the SMEI ICME data and predict their times of arrival at Earth. They then compared these predicted ICME arrival times with the actual shock times at L1, and we resorted their results to produce the time difference histogram of Figure 8.

[65] In this study as stated earlier, we converted the LASCO CME and SMEI ICME ε-time data to distance-time by assuming that the ICME was launched from the CDAW-identified source location and then propagated radially away from the Sun. This is related to the "fixed Φ" method described by *Howard et al.* [2007] and *Kahler and Webb* [2007]. Figures 2 (bottom), 6 (bottom), and 11c are examples of these distance-time plots. We made no assumptions about the speed or acceleration of the ICME. We do implicitly make the assumption that both LASCO and SMEI are tracking the same front of material as it moves out. Despite the difficulties that can be raised with each of these assumptions, our goal here is merely to estimate the uncertainties in arrival times that such straightforward assumptions would yield.

[66] To determine the distances it was necessary to attempt to correct for the projection effects that are typical of solar and heliospheric images and, thus, to convert the angular distance to a "true" 3-D distance. This was done using the following equation from *Howard et al.* [2007, section 3.1]:

$$1/R = \sin\alpha \cot\varepsilon + \cos\alpha, \tag{1}$$

where R is the distance of the measured point from the Sun in AU, ε is the elongation angle, and α is the angle subtended by the measured point at the Sun. In terms of the heliocentric-ecliptic colatitude θ and longitude Φ,

$$\cos\alpha = \sin\theta \cos\Phi. \tag{2}$$

The θ and Φ coordinates were obtained from the heliographic location of the surface feature that CDAW WG1 associated with each LASCO CME, flare, active region, etc., as given in the Source Location column of Table 2.

[67] On each of the (3-D) distance-time plots for the CDAW events we then fit the SMEI ICME data points with a best fit linear solution and extrapolated that line to 1 AU. This 1 AU crossing time, given in the Predicted 3-D column of Table 2, then represents the "arrival time" of the ICME front at 1 AU. This time can then be compared with the actual shock AT at 1 AU from the Shock column of Table 2 and the algebraic differences tabulated as shown by *Howard et al.* [2006, Table 3]. In our case we also compared the SMEI ICME arrival time in the Predicted 3-D column with the storm onset time in the *Dst* Date column. These times and their differences are given in Table 3. (This fitting procedure can also be used to estimate a projected ICME onset time at 0 AU, i.e., at the Sun, and the ICME speed. However, we did not use those values in this study.)

[68] The time differences are given in the ΔT ICME-Shock and ΔT Storm-ICME columns of Table 3 for the shock-ICME AT and storm onset-ICME AT, respectively. In the ΔT ICME-Shock column, the plus sign means that the ICME arrived after the shock, and in the ΔT Storm-ICME column that the storm onset followed ICME arrival. This ordering was adopted on the basis of the expected standoff

Table 3. SMEI Data-Based Predictions of ICME Arrival Times at 1 AU

CDAW Storm	Shock Arrival Date and Time (UT)	Storm Onset Date and Time (UT)	SMEI ICME Arrival Date and Time (UT)	ΔT ICME-Shock (hour)	ΔT Storm-ICME (hour)
			2003		
63	29 May, 1155; 29 May 1831	29 May, 2200	29 May, 2134; 19 May, 2238	+3.05, +4.1	+0.4, −0.4
66	17 Aug., 1345	17 Aug., 2300	18 Aug., 0705	+17.3	−15.9
67	29 Oct., 0558	29 Oct., 1500	29 Oct., 1214; 29 Oct., ~2000	+6.25, +14.0	+2.75, −5.0
69	20 Nov., 0835	20 Nov., 1100	19 Nov., 1939; 20 Nov., 1836	−12.9, +10.0	+15.35, −7.6
			2004		
70	22 Jan., 0105	22 Jan., 1200	22 Jan., ~0100; 22 Jan., 1706	0.0, +16.0	+11.0, −5.1
72	3 Apr., 0900	3 Apr., 1800	2 Apr., 1634; 3 Apr., 0910; 3 Apr., 2339; 4 Apr., 0445	−16.4, 0.0, +14.65, +19.75	+25.4, +8.8, −5.65, −10.75
73	22 Jul., 0945	22 Jul., 2300	22 Jul., 1732; 22 Jul., 2251	+7.75, +13.4	+5.5, +0.15
77	7 Nov., 0156; 7 Nov., 1759	7 Nov., 2200	7 Nov., 0324	+1.5, −14.6	+18.6
78	9 Nov., 0925	10 Nov., 1000	9 Nov., 0537; 9 Nov., 1643	−3.8, +7.3	+28.4, +17.3
			2005		
79	17 Jan., 0715	17 Jan., ~1800	17 Jan., 2152; 18 Jan., 0240	+14.6, +19.4	−3.9, −8.7
80	21 Jan., 1652	21 Jan., 2100	21 Jan., 0420; 22 Jan., 0427	−12.5, +11.6	+16.7, −7.45
86	24 Aug., 0545	24 Aug., 1000	24 Aug., 1919	+13.6	−9.3
88	11 Sep., 0100	11 Sep., 0300	11 Sep., 0557	+4.95	−2.95
			2006		
–	14 Dec., 1357	15 Dec., 0000	14 Dec., 1629	+2.55	+7.5
Mean				+5.44 (26)	+3.01 (25)
RMS				±10.48	±11.95

distance between an IP shock and its ejecta and the shock–SMEI auroral onset – storm onset sequence found above. Note that there can be more than one entry per CDAW storm on the basis of multiple shocks (77) or the tracking of multiple ICMEs by SMEI prior to the storm. For space weather prediction purposes we chose not to interpret which ICME was best associated with the storm, but to group them together to find an uncertainty in their predicted ATs. In a sense this is a worst case scenario but one that a forecaster might typically confront given only hours to make a storm forecast. We calculated the algebraic mean of these time difference distributions and found them to be +5.44 and +3.01 hours, respectively, for ICME AT-shock and storm onset-ICME AT. Thus, on average for each event, the AT of the shock was followed 5.4 hours later by the AT of the ICME, which was followed 3.0 hours later by storm onset.

[69] We can now compare our results with those from *Howard et al.*'s [2006] study, which was based on the time differences (Figure 8) between predicted (LASCO CMEs and SMEI ICMEs) and actual (ACE shocks) arrival times for 15 events associated with storms having a range of peak *Dst* values. The algebraic mean for ICME AT shock we calculated for that study was +4.0 hours. This value is reasonably consistent with the +5.4 hours we found for this study.

[70] A much debated subject in space weather research is the accuracy with which the geoeffective ICME AT can be predicted by a given procedure or model. This is usually given statistically as a range or uncertainty in hours for a given set of ATs. Quantitatively, this can be stated in terms of the standard deviation, or RMS of a set of predicted versus actual ATs. From Table 3, the RMS values for the ICME-shock and storm-ICME time differences were ±10.48 and ±11.95 hours, respectively. (Again, these "uncertainties" are relative to the average ICME transit time of 54 hours.) The ICME-shock RMS time difference from *Howard et al.*'s [2006] study was ±11.4 hours; thus, our results for the CDAW storms show an improved accuracy by about one hour versus *Howard et al.*'s [2006] study. Although *Howard et al.* [2006] used a different range of storms, perhaps the main reason for this difference is that they converted SMEI ICME elongation to distance using the point P approximation whereas we used the "fixed Φ" method.

[71] Our uncertainty result using SMEI data to predict ICME AT, and therefore storm onset, of ±10.5 hours represents an improvement over similar values published in the literature. These include (1) ~±16 hours by *Gopalswamy et al.* [2001] (Note that they quoted a mean error of 10.7 hours; this is not the RMS, which we estimate as about ±16 hours); (2) ±12.0 (HAFv2), 12.6 (ICME-ICME), and 11.4 hours (ICME-IP) by *Cho et al.* [2003]; (3) ±12.2 (STOA), 11.2 (ISPM), and 11.6 hours (HAFv2) by *Fry et al.* [2003]; (4) ±14 hours by *Schwenn et al.* [2005]; and (5) ±11.7 (STOA), 11.0 (ISPM), and 11.5 hours (HAFv2) by *McKenna-Lawlor et al.* [2006].

[72] Thus, these results demonstrate that the SMEI observations can be used to improve forecasting skill in predicting the arrival of potentially geoeffective solar wind disturbances at Earth. However, our analysis is limited in that it that it used only events known to be associated with intense geomagnetic storms and, therefore, by definition it cannot include 'correct null' predictions. The sample size is also small. To properly evaluate forecast skill using

standard, e.g., meteorological metrics, it would be necessary to conduct a double-blind test on a statistically significant sample of events without a priori knowledge of an associated storm. This is beyond the scope of this study.

4.2.2. Attempted Near-Real-Time Forecasting With SMEI

[73] SMEI has demonstrated its ability to track CMEs from near the Sun to Earth, thus providing a new capability for forecasting the occurrence of storms. SMEI was able to detect a number of geoeffective ICMEs at elongations of 20–30° (from Sun center), or estimated distances as far away as 2/3 of the distance between the Sun and Earth. Depending on the speed of the ICME front, these distances would correspond to lead times of 10 hours to 1–2 days. SMEI was not designed to be an operational mission, so we were usually unable to use the SMEI data to attempt near-real-time forecasts. Therefore, all of the studies discussed in this paper were retrospective in nature.

[74] However, because of improved circumstances such as an improved data latency later in the mission, we were able to produce near-real-time predictions using LASCO and SMEI data for two storms. The first was CDAW 77 in early November 2004 (see Figures 5 and 6). In an AFRL email issued on 7 November at 2300 UT, one of us, DRM, predicted the Earth arrival of the ICME observed by SMEI on 6–7 November to be ~12:00 on 7 November. Quicklook SMEI images also showed brightening aurora at 1400 UT, indicating to DRM imminent storm onset even before the written email alert. The ICME was correctly attributed to the first of the two LASCO halo CMEs observed on 4 November (Table 2). In an email two hours later we noted that the ACE data indicated "a possible shock and ejecta and a storm with $Kp = 7$ late on 7 November" with storm onset at 2200 UT. This was about the time of the email prediction; when first observed the ICME was already at ~80° ε, providing little advance warning time. However, we note that our predicted AT on the basis of the current $d-t$ plot (Figure 6) was even earlier, 0324 UT, on 7 November.

[75] SMEI observed and tracked two eastern ICMEs on 2 and 4 January 2008 associated with a solar east limb active region and CMEs observed by LASCO on 31 December and 2 January, respectively. One of us, TAK, used the SMEI ε-time plots to predict their 1 AU crossing times to be 3 January at 1500 UT and 5 January at 0030 UT, in emails on 3 January at 1441 UT and 4 January at 1536 UT. Because of the ICMEs' east limb sources, we did not expect storms to occur at Earth and indeed there were none. Thus, these constitute "null" predictions. There was possible ICME material observed in the ACE data embedded in a sector boundary crossing early on 5 January, in agreement with the SMEI predicted AT.

5. Discussion: A New Capability for Forecasting Space Weather

[76] SMEI began routine observations in February 2003, and has maintained an average duty cycle of 85% to the present. This period covers the CDAW storms 63–88 occurring from May 2003 to October 2005. There was a long outage of SMEI data from 28 April to 8 June 2005, resulting in a lack of SMEI data for CDAW storms 81–84. However, SMEI was able to observe the associated ICMEs for most of the other CDAW intense storms. We described the SMEI observations and analyses for the 26 CDAW storms, numbers 63–88, that occurred during the SMEI observations from May 2003 to October 2005 as well as for the two other intense storms that occurred after that period through the end of 2007, for a total of 28 storms considered.

[77] The main statistical results of this study are summarized in Appendix A. We studied the 18 CDAW storms with adequate SMEI coverage and for which CDAW WG1 identified the solar and IP sources. Of these 18 storms, 12 were preceded by a definitely associated SMEI ICME, four by a likely associated ICME, and two had no associated ICME. Thus, we conclude that SMEI likely detected and tracked 89% (16/18) of the ICMEs that caused these storms.

[78] The typical pattern for these intense events was IP shock, SMEI aurora onset, storm onset, with each interval about four hours in length. The mean time difference between when SMEI first observed the ICME and the SMEI aurora onset time was 23.2 hours (range 7–36 hours). The mean time difference between when SMEI first observed the ICME and the storm onset time was 27.5 hours (range 14–44 hours). Therefore, on average SMEI is capable of the first detection of a geoeffective ICME ~1 day in advance, yielding a prediction lead time of ~18 hours but with a large range. Since a forecaster requires about 6 hours of SMEI data to input into an arrival time prediction program, the resultant warning time is reduced to an average of ~18 hours. Of course, the time differences ranged over a factor of five, so the actual lead time will be better or worse than this, depending on the speed and brightness of each event.

[79] Using our method for converting elongation to distance, we were able to make a prediction of the ICME arrival time at 1 AU for each event and to calculate the time differences for two sets of data: the time between shock and ICME arrival times, and the time between the ICME arrival time and the storm onset. On average for each event, the AT of the shock was followed 5.4 hours later by the AT of the ICME, which was followed 3.0 hours later by storm onset. The algebraic mean for the ICME AT shock time differences from *Howard et al.*'s [2006] study was +4.0 hours, which was reasonably consistent with the +5.4 hours we found for this study.

[80] These results suggest the following basic scheme for using SMEI-type observations to make storm forecasts. When a solar eruption occurs on the frontside, especially if within ~45 heliodegrees of Sun center, a forecaster should check if an associated CME is observed by a coronagraph within a reasonable time window. If so, and especially if the CME is a partial or full halo, the forecaster can then check the SMEI observations a day or so later, depending on the apparent speed of the initial CME, for any possibly associated ICMEs. If one is found, then the leading edge is measured over several successive frames and an elongation

versus time plot constructed. For SMEI we recommend that a minimum of three data points, thus over three orbits or ~6 hours, are necessary for such a plot. Then, assuming the solar source location and onset time of the CME and that it propagates radially, a distance-time relation can be calculated and extrapolated to the 1 AU distance. The storm onset time will then be predicted to be ~3 hours after this 1 AU arrival time. The prediction program can be rerun and the predicted 1 AU AT updated as more *e-t* data points become available to the forecaster. Note that actual *e-t* and *d-t* plots are not needed, but they will be helpful in confirming the predicted AT with solar wind and geomagnetic data such as we have shown in this paper.

[81] Of course, there are some limitations to making such forecasts. If no associated ICME is detected by the imager, then no useful forecast can be made. This could lead to a missed forecast if there is a geoecffective ICME that is not detected (or not detected in time) by the imager. In addition, a SMEI-type imager cannot measure magnetic fields and, therefore, even if an ICME is detected, the strength and orientation of the magnetic field within or ahead of it would remain unknown. However, this is more likely to cause uncertainty in the intensity of a storm, rather than no storm at all, because most ICMEs tend to have geoeffective southward fields somewhere ahead of or within themselves. We also note that our analysis was limited in that the sample size was small and its analysis was in only one direction, from intense storms back to their solar sources.

[82] The RMS range between model or procedure predicted and actual geoeffective ICME ATs is often used as a measure of the uncertainty in the procedure or model. We calculated the RMS values for the ICME-shock and storm-ICME time differences of our study which were ±10.48 and ±11.95 hours, respectively (relative to the average ICME transit time of 54 hours). The ICME-shock RMS time difference from *Howard et al.*'s [2006] study was ±11.4 hours; thus, our results for the CDAW storms show an improved accuracy by about 1 hour compared to *Howard et al.*'s [2006] study and other similar studies in the literature. Although one can argue that one hour is of the order of the observational cadence of both ACE and SMEI, our results remain comparable to other studies and, therefore, demonstrate an improvement. We believe that much of this improvement is because we had available to us the CDAW source region information for each event that allowed us to convert the SMEI ICME elongations to distances using the "fixed Φ" method. *Howard et al.* [2006] used the "point P" method. We note that with SMEI imagery alone we do not know which part(s) of the shock/sheath/ejecta ensemble we are observing in any given event or whether solar wind material accumulated with a snowplow-type of action plays a role. In addition, the methods in the other studies differed somewhat in whether only shocks, or shocks versus ICMEs, or CMEs versus ICMEs were compared for arrival times. However, given the large distances and travel times involved, we do not think that the few hours differences between shock and ejecta arrival times significantly biases our result compared to the others.

[83] Interplanetary coronal mass ejections (ICMEs) are a primary cause of severe space weather at Earth because they drive shocks and trigger geomagnetic storms that can damage spacecraft and ground-based systems. The SMEI experiment has detected geoeffective ICMEs at ~1/3 of the distance from the Sun to Earth and beyond, corresponding to an average advance warning time of ~1 day (relative to the average ICME transit time of 2.2 days). SMEI's images of ICMEs, obtained with a cadence of ~100 min, provide a dynamic view of ICME morphology along trajectories aimed toward Earth. Our investigations of ICME intensity, structure evolution and kinematics should improve our ability to forecast storm effects at Earth.

[84] Detecting and tracking ICMEs in this distance range is a new capability that, when combined with other space environment sensors and physics-based heliospheric models, promises to greatly enhance our ability to forecast and study space weather. The SMEI allows near-real-time tracking of ICMEs as they propagate outward from the Sun through the heliosphere. Above we outlined a very simple approach, using only solar and SMEI data, which a forecaster might use to predict ICME arrival at 1 AU and storm onset at Earth. STEREO is now providing a similar capability from two unique vantage points.

Appendix A: Statistical Results of SMEI-CDAW Storm Study

[85] The main statistical results from study of the CDAW storms that involved SMEI data are listed here and summarized in section 5.

A1. CDAW Storm: ICME Associations

[86] Of the 28 CDAW storms studied, 7 had no or inadequate SMEI data, and 3 more were identified as CIR driven. Of the remaining 18 storms with adequate SMEI coverage and for which CDAW WG1 identified the solar and IP sources, 12 were preceded by a definitely associated SMEI ICME, four by a likely associated ICME, and two had no associated ICME. In addition, for these 18 storms, 9 of the LASCO CMEs and SMEI ICMEs were likely, 5 possibly, 3 questionably, and 1 unlikely associated.

A2. SMEI ICME Spans and Elongations

[87] The ICME spans were measured from the SMEI data and are presented in Table 2. The mean value was 78.63° and the range was 30–13°. There were 11 measured values and for an additional 5 we could only measure lower limits. The elongation angles of the ICMEs at the time of the onset of each storm are presented in Table 2. The mean value was 78.67° and the range was 45–105°. There were 15 measured values.

A3. Timing Results

[88] The observed time differences, ΔT, between the onset time of each storm and the onset time of the SMEI aurora are listed in Table 2 (column t_{diff} St-Au). The mean

value was +4.085 hours, and the range was −2.5 – 8.15 hours. There were 10 measured values. The observed time differences, ΔT, between the onset time of each SMEI aurora and the shock arrival time at 1 AU are listed in Table 2, column 19. The mean value was +3.88 hours, and the range was −22.9 to +15.4 hours. There were 14 measured values and for an additional 4 we could only measure lower limits. There were only three events in which the shock preceded the aurora onset.

[89] The typical sequence of these three key events was the arrival at 1 AU of the IP shock, onset of the SMEI aurora, and onset of the storm. From above, each of these time intervals was about four hours in duration. The mean time difference, ΔT, between when SMEI first observed the ICME and the onset of the SMEI aurora was 23.23 hours, with a range of 7 – 36 hours (Table 2 column t_{diff} Au-FO). There were 11 measured values. The mean time difference between when SMEI first observed the ICME and the storm onset time was 27.53 hours, with a range of 14 – 44 hours (Table 2 column t_{diff} Au-FO). There were 15 measured values.

[90] Using our method for converting measured SMEI elongation angles to distance, we could predict the ICME arrival time at 1 AU for each event and use it to calculate the time differences for two sets of data: the time between shock and ICME arrival times (ATs), and the time between the ICME arrival time and the storm onset. These results are given in Table 3. The mean value between the AT of the shock and the AT of the ICME was +5.44 hours. The mean value between the storm onset and the AT of the ICME was +3.01 hours. Thus, the typical sequence began with the arrival of the shock, followed 5.4 hours later by the predicted arrival of the ICME, followed 3.0 hours later by the onset of the storm.

[91] The RMS range between model- or procedure-predicted and actual geoeffective ICME ATs is often used as a measure of the uncertainty in the procedure or model. The RMS value for the ICME-shock time differences was ±10.48 hours, with 26 values. The RMS value for the storm-ICME time differences was ±11.95 hours, with 25 values.

[92] **Acknowledgments.** We are grateful to the organizers of the NASA LWS Geostorm Coordinated Data Analysis Workshop, especially to the members of Working Group 1 on Drivers of Geomagnetic Storms for their many hours spent in studying and identifying the solar and interplanetary sources of the storms. We also acknowledge use of the CME catalog that is generated and maintained at the CDAW Data Center by NASA and The Catholic University of America in cooperation with the Naval Research Laboratory. SOHO is a project of international cooperation between ESA and NASA. We thank E. Cliver of AFRL for comments on the manuscript. We acknowledge P. Hick and A. Buffington for their efforts in the calibration and processing of the SMEI data at UCSD. SMEI is a collaborative project of the U.S. Air Force Research Laboratory, NASA, the University of California at San Diego, the University of Birmingham (U. K.), Boston College, and Boston University. Financial support has been provided by the Air Force, the University of Birmingham, and NASA. An overview of the SMEI instrument can be found on the Internet at http://www.kirtland.af.mil/shared/media/document/AFD-070404-102.pdf, and current and archival images and movies and presentations at http://smei.nso.edu/. This work was supported for each coauthor by the following sources: T.A.H. by the National Research Council Fellowship Program, funded by AFOSR contract F49620-02C-0015; B.V.J. at UCSD by AFRL contract FA8718-04-C-0050, NSF grant ATM-0331513 and NASA grant NNG05GM58G; D.F.W., T.A.K., and D.R.M. at Boston College by AFRL contract FA8718-06-C-0015; S.J.T. under contract F61775-02-WE043 to the University of Birmingham; and C.D.F. at EXPI by AURA contract C10562N. The authors also were supported by NASA grant NNGO5GF98G.

References

Arge, C. N., and V. J. Pizzo (2000), Improvement in the prediction of solar wind conditions using near-real time solar magnetic field updates, *J. Geophys. Res.*, *105*, 10,465 – 10,4798, doi:10.1029/1999JA000262.

Arge, C. N., J. G. Luhmann, D. Odstrcil, C. J. Schrijver, and Y. Li (2004), Stream structure and coronal sources of the solar wind during the May 12th, 1997 ICME, *J. Atmos. Sol. Terr. Phys.*, *66*, 1295 – 1309.

Billings, D. E. (1966), *A Guide to the Solar Corona*, Academic, San Diego, Calif.

Cho, K. S., Y. J. Moon, M. Dryer, C. D. Fry, Y. D. Park, and K. S. Kim (2003), A statistical comparison of interplanetary shock and ICME propagation models, *J. Geophys. Res.*, *108*(A12), 1445, doi:10.1029/2003JA010029.

Cliver, E. W., J. Freynman, and H. B. Garrett (1990), An estimate of the maximum speed of the solar wind, 1938 – 1989, *J. Geophys. Res.*, *95*, 17,103 – 17,112.

Craven, J. D., et al. (1985), The global auroral response to magnetospheric compressions by shocks in the solar wind, *J. Geomagn. Geoelectr.*, *37*, 367 – 380.

Egeland, A., et al. (1994), Ground and satellite observations of postdawn aurorae near the time of a sudden storm commencement, *J. Geophys. Res.*, *99*, 2095 – 2108, doi:10.1029/92JA03027.

Eyles, C. J., G. M. Simnett, M. P. Cooke, B. V. Jackson, A. Buffington, P. P. Hick, N. R. Waltham, J. M. King, P. A. Anderson, and P. E. Holladay (2003), The Solar Mass Ejection Imager (SMEI), *Sol. Phys.*, *217*, 319 – 347, doi:10.1023/B:SOLA.0000006903.75671.49.

Fry, C. D., W. Sun, C. S. Deehr, M. Dryer, Z. Smith, S.-I. Akasofu, M. Tokumaru, and M. Kojima (2001), Improvements to the HAF solar wind model for space weather predictions, *J. Geophys. Res.*, *106*, 20,985 – 21,001, doi:10.1029/2000JA000220.

Fry, C. D., M. Dryer, C. S. Deehr, W. Sun, S.-I. Akasofu, and Z. Smith (2003), Forecasting solar wind structures and shock arrival times using an ensemble of models, *J. Geophys. Res.*, *108*(A2), 1070, doi:10.1029/2002JA009474.

Fry, S. E., C. D. Fry, and T. A. Howard (2006), Combining HAFv2 model simulations with SMEI images to improve ICME forecasts and interpretations of observations, *Eos Trans. AGU*, *87*(52), Fall Meet. Suppl., Abstract SH33A-0395.

Gopalswamy, N., A. Lara, S. Yashiro, M. Kaiser, and R. A. Howard (2001), Predicting the 1-AU arrival times of coronal mass ejections, *J. Geophys. Res.*, *106*, 29,207 – 29,218, doi:10.1029/2001JA000177.

Hakamada, K., and S.-I. Akasofu (1982), Simulation of three-dimensional solar wind disturbances and resulting geomagnetic storms, *Space Sci. Rev.*, *31*, 3 – 70, doi:10.1007/BF00349000.

Hick, P. P., A. Buffington, and B. V. Jackson (2005), The SMEI real-time data pipeline: From raw CCD frames to photometrically accurate full-sky maps, *Proc. SPIE*, *5901*, 340 – 346, doi:10.1117/12.617996.

Howard, T. A., and G. M. Simnett (2008), Interplanetary coronal mass ejections that are undetected by solar coronagraphs, *J. Geophys. Res.*, *113*, A08102, doi:10.1029/2007JA012920.

Howard, T. A., D. F. Webb, S. J. Tappin, D. R. Mizuno, and J. C. Johnston (2006), Tracking halo coronal mass ejections from 0 – 1 AU and space weather forecasting using the Solar Mass Ejection Imager (SMEI), *J. Geophys. Res.*, *111*, A04105, doi:10.1029/2005JA011349.

Howard, T. A., C. D. Fry, J. C. Johnston, and D. F. Webb (2007), On the evolution of coronal mass ejections in the interplanetary medium, *Astrophys. J.*, *667*, 610 – 625, doi:10.1086/519758.

Jackson, B. V., et al. (2004), The Solar Mass Ejection Imager (SMEI): The mission, *Sol. Phys.*, *225*, 177 – 207, doi:10.1007/s11207-004-2766-3.

Jackson, B. V., A. Buffington, P. P. Hick, X. Wang, and D. Webb (2006), Preliminary three-dimensional analysis of the heliospheric response to the 28 October 2003 ICME using SMEI white-light observations, *J. Geophys. Res.*, *111*, A04S91, doi:10.1029/2004JA010942.

Jackson, B. V., P. P. Hick, A. Buffington, M. M. Bisi, and E. A. Jensen (2007), SMEI observations in the STEREO era, *Proc. SPIE*, *6689*, 1 – 14, doi:10.1117/12.734870.

Jackson, B. V., M. M. Bisi, P. P. Hick, A. Buffington, J. M. Clover, and W. Sun (2008), Solar Mass Ejection Imager 3-D reconstruction of the 27 – 28 May 2003 CME sequence, *J. Geophys. Res.*, *113*, A00A15, doi:10.1029/2008JA013224.

Johnston, J. C., J. B. Mozer, R. R. Radick, P. E. Holladay, T. A. Kuchar, D. R. Mizuno, and D. F. Webb (2004), Heliospheric imagers for tracking coronal mass ejections: Lessons learned from the Solar Mass Ejection Imager, *Eos Trans. AGU*, *85*(47), Fall Meet. Suppl., Abstract SH11A-08.

Kahler, S. W., and D. F. Webb (2007), V arc interplanetary coronal mass ejections observed with the Solar Mass Ejection Imager, *J. Geophys. Res.*, *112*, A09103, doi:10.1029/2007JA012358.

Loewe, C. A., and G. W. Prolss (1997), Classification and mean behavior of magnetic storms, *J. Geophys. Res.*, *102*, 14,209 – 14,213, doi:10.1029/96JA04020.

McKenna-Lawlor, S. M. P., M. Dryer, M. D. Kartalev, Z. Smith, C. D. Fry, W. Sun, C. S. Deehr, K. Kecskemety, and K. Kudela (2006), Near real-time predictions of the arrival at Earth of flare-related shocks during Solar Cycle 23, *J. Geophys. Res.*, *111*, A11103, doi:10.1029/2005JA011162.

Mizuno, D., et al. (2005), Very high-altitude aurora observations with the Solar Mass Ejection Imager, *J. Geophys. Res.*, *110*, A07230, doi:10.1029/2004JA010689.

Richardson, I. G., and H. V. Cane (2004), Identification of interplanetary coronal mass ejections at 1 AU using multiple solar wind plasma composition anomalies, *J. Geophys. Res.*, *109*, A09104, doi:10.1029/2004JA010598.

Richardson, I. G., et al. (2006), Major geomagnetic storms ($Dst \leq -100$ nT) generated by corotating interaction regions, *J. Geophys. Res.*, *111*, A07S09, doi:10.1029/2005JA011476.

Richardson, I. G., et al. (2007), Correction to ''Major geomagnetic storms (Dst ≤ -100 nT) generated by corotating interaction regions'', *J. Geophys. Res.*, *112*, A12105, doi:10.1029/2007JA012332.

Schwenn, R., A. Dal Lago, E. Huttunen, and W. D. Gonzalez (2005), The association of coronal mass ejections with their effects near the Earth, *Ann. Geophys.*, *23*, 1033 – 1059.

Sun, W., C. S. Deehr, C. D. Fry, M. Dryer, Z. Smith, and S.-I. Akasofu (2008), Simulation of the SMEI and ''STEREO-like'' views of the solar wind following the solar flares of 27 – 29 May 2003, *Space Weather*, *6*, S03006, doi:10.1029/2006SW000298.

Tappin, S. J., et al. (2004), Tracking a major interplanetary disturbance with SMEI, *Geophys. Res. Lett.*, *31*, L02802, doi:10.1029/2003GL018766.

Tsurutani, B. T., and W. D. Gonzales (1997), The interplanetary causes of magnetic storms: A review, in *Coronal Mass Ejections*, *Geopyhs. Monogr. Ser.*, vol. 99, edited by N. Crooker, J. Joselyn, and J. Feynman, pp. 77 – 89, AGU, Washington, D. C.

Vourlidas, A., and R. A. Howard (2006), The proper treatment of coronal mass ejection brightness: A new methodology and implications for observations, *Astrophys. J.*, *642*, 1216 – 1221, doi:10.1086/501122.

Webb, D., and J. Allen (2004), Spacecraft and ground anomalies related to the October – November 2003 solar activity, *Space Weather*, *2*, S03008, doi:10.1029/2004SW000075.

Webb, D. F., et al. (2006a), Solar Mass Ejection Imager (SMEI) observations of ICMEs in the heliosphere, *J. Geophys. Res.*, *111*, A12101, doi:10.1029/2006JA011655.

Webb, D. F., T. Howard, J. Johnston, and C. Fry (2006b), SMEI observations and space weather forecasting, *Eos. Trans. AGU*, *87*(52), Fall Meet. Suppl., Abstract SH33A-0394.

Yashiro, S., N. Gopalswamy, G. Michalek, O. C. St.Cyr, S. P. Plunkett, N. B. Rich, and R. A. Howard (2004), A catalog of white light coronal mass ejections observed by the SOHO spacecraft, *J. Geophys. Res.*, *109*, A07105, doi:10.1029/2003JA010282.

Zhang, J., et al. (2007a), Solar and interplanetary sources of major geomagnetic storms ($Dst \leq -100$ nT) during 1996 – 2005, *J. Geophys. Res.*, *112*, A10102, doi:10.1029/2007JA012321.

Zhang, J., et al. (2007b), Correction to ''Solar and interplanetary sources of major geomagnetic storms ($Dst \leq -100$ nT) during 1996 – 2005'', *J. Geophys. Res.*, *112*, A12103, doi:10.1029/2007JA012891.

C. D. Fry, Exploration Physics International, Inc., 425 Springhill Road NW, Huntsville, AL 35806, USA.

T. A. Howard, Air Force Research Laboratory, National Solar Observatory, 3010 Coronal Loop, Sunspot, NM 88349, USA.

B. V. Jackson, Center for Astrophysics and Space Science, University of California, San Diego, 9500 Gilman Drive, Box 0424, La Jolla, CA 92093-0424, USA.

J. C. Johnston, T. A. Kuchar, D. R. Mizuno, and D. F. Webb, Space Vehicles Directorate, Air Force Research Laboratory, Hanscom Air Force Base, MA 01731, USA. (david.webb.ctr@hanscom.af.mil)